universe

MDPI

Article

Binary Black Hole Spins: Model Selection with GWTC-3

Carole Périgois [1,2,*], Michela Mapelli [1,2,3,*], Filippo Santoliquido [1,2,4], Yann Bouffanais [1,2] and Roberta Rufolo [1]

1 Physics and Astronomy Department Galileo Galilei, University of Padova, Vicolo dell'Osservatorio 3, 35122 Padua, Italy
2 INFN—Padova, Via Marzolo 8, 35131 Padua, Italy
3 Institut für Theoretische Astrophysik, Zentrüm für Astronomie, Albert-Ueberle-Strasse 2, 69120 Heidelberg, Germany
4 Gran Sasso Science Institute (GSSI), 67100 L'Aquila, Italy
* Correspondence: caroleperigois@outlook.com (C.P.); mapelli@uni-heidelberg.de (M.M.)

Abstract: The origin of the spins of stellar-mass black holes is still controversial, and angular momentum transport inside massive stars is one of the main sources of uncertainty. Here, we apply hierarchical Bayesian inference to derive constraints on spin models from the 59 most confident binary black hole merger events in the third gravitational-wave transient catalogue (GWTC-3). We consider up to five parameters: chirp mass, mass ratio, redshift, effective spin, and precessing spin. For the model selection, we use a set of binary population synthesis simulations spanning drastically different assumptions for black hole spins and natal kicks. In particular, our spin models range from the maximal to minimal efficiency of angular momentum transport in stars. We find that if we include the precessing spin parameter into our analysis, models predicting only vanishingly small spins are in tension with GWTC-3 data. On the other hand, models in which most spins are vanishingly small but that also include a subpopulation of tidally spun-up black holes are a good match to the data. Our results show that the precessing spin parameter has a crucial impact on model selection.

Keywords: black hole physics; gravitational waves; binaries; general; stars; black holes

Citation: Périgois, C.; Mapelli, M.; Santoliquido, F.; Bouffanais, Y.; Rufolo, R. Binary Black Hole Spins: Model Selection with GWTC-3. *Universe* **2023**, *9*, 507. https://doi.org/10.3390/universe9120507

Academic Editor: Lorenzo Iorio

Received: 5 September 2023
Revised: 15 November 2023
Accepted: 21 November 2023
Published: 5 December 2023

1. Introduction

The third observing run (O3) of the Advanced LIGO [1] and Virgo [2] detectors has brought the number of compact binary merger observations up to 90 events with a probability of astrophysical origin > 0.5 [3–6]. The intrinsic distribution of primary black hole (BH) masses inferred by the LIGO–Virgo–KAGRA collaboration (hereafter, LVK) shows several substructures, including a main peak at $\approx$10 $M_\odot$, a secondary peak at $\approx$30–40 $M_\odot$, and a long tail extending up to $\sim$80 $M_\odot$, e.g., [7]. The inferred distribution of mass ratios has a strong preference for equal-mass systems, but several BBHs are confidently unequal-mass systems (e.g., GW190412 [8]; GW190517 [4]). The analysis of LVK data safely excludes that all BHs are maximally spinning [3,9,10]. Typical spin magnitudes in BBHs are small, with $\sim$50% of BHs having $\chi \lesssim 0.3$, e.g., [4,11], although not all BHs in the LVK sample have zero spin [12,13]. For example, GW151226 [14] and GW190517 [7] confidently possess spin. LVK data also support some mild evidence for spin–orbit misalignment, e.g., [4,7,15–20].

These results provide crucial insights to understand BBH formation and evolution, e.g., [10–12,21–46]. Moreover, the mass and spin of BHs carry the memory of their progenitor stars and therefore are a key to unravel the details of massive star evolution and collapse, e.g., [47–67]. In particular, the spin magnitude of a stellar-origin BH should retain the imprint of the spin of the core of its progenitor star, e.g., [56,57,68–72].

Several models have been proposed to infer the spin magnitude of a BH from that of the progenitor star. The main open question concerns the efficiency of angular momentum transport within a star, e.g., [73–75]. If angular momentum is efficiently transferred from the core to the outer layers, mass loss by stellar winds can dissipate most of it, leading to a low-spinning stellar core and then to a low-spinning BH. If instead the core retains most of its initial angular momentum until the final collapse, the BH will be fast spinning.

In the shellular model [76–79], angular momentum is mainly transported by meridional currents and shear instabilities, leading to relatively inefficient spin dissipation. In contrast, according to the Tayler–Spruit dynamo mechanism [80], the differential rotation induces the formation of an unstable magnetic field configuration, leading to an efficient transport of angular momentum via magnetic torques. Building upon the Tayler–Spruit mechanism, Fuller et al. 2019 [70] derived a new model with an even more efficient angular momentum dissipation, predicting that the core of a single massive star might end its life with almost no rotation.

Electromagnetic observations yield controversial results. Asteroseismology favours slowly rotating cores in the late evolutionary stages, but the vast majority of stars with an asteroseismic estimate of the spin are low-mass stars [81–83]. The continuum-fitting derived spins of BHs in high-mass X-ray binaries are extremely high, e.g., [84–86], but such measurements might be affected by substantial observational biases, e.g., [84]. Finally, BH spins inferred from quasi-periodic oscillations yield notably smaller values than continuum fitting. For example, the estimate of the dimensionless spin of the BH in GRO J1655–40 is $\chi = 0.7 \pm 0.1$ and 0.290 ± 0.003 from continuum fitting [87] and quasi-periodic oscillations [88], respectively.

In a binary system, the evolution of the spin is further affected by tidal forces and accretion, which tend to spin up a massive star, whereas nonconservative mass transfer and common-envelope ejection enhance mass loss, leading to more efficient spin dissipation [68,89–91]. For example, the model by Bavera et al. (2020, [56]) shows that the second-born BH can be highly spinning if its progenitor was tidally spun up when it was a Wolf–Rayet (WR) star orbiting about the first-born BH.

Furthermore, the orientation of the BH spin with respect to the orbital angular momentum of the binary system encodes information about binary evolution processes. In a tight binary system, tides and mass transfer tend to align the stellar spins with the orbital angular momentum ([92], but see Stegmann et al. 2021 [93] for a possible spin-flip process induced by mass transfer). If the binary system is in the field, the supernova kick is the main mechanism that can misalign the spin of a compact object with respect to the orbital angular momentum, by tilting the orbital plane, e.g., [94]. Finally, the spins of BHs in dynamically formed binary systems are expected to be isotropically distributed, because close encounters in a dense stellar cluster reset any previous signature of alignment, e.g., [23,41].

Here, we perform a model-selection hierarchical Bayesian analysis on confident LVK BBHs ($p_{\rm astro} > 0.9$ and FAR $< 0.25\,{\rm yr}^{-1}$). We consider models of field BBHs for three of the most used angular-momentum transport models: (i) the shellular model as implemented in the Geneva stellar evolution code [77], (ii) the Tayler–Spruit dynamo model as implemented in the MESA code [74], and (iii) the model by Fuller et al. (2019, [70]). Hereafter, we refer to these three models simply as GENEVA (G), MESA (M), and FULLER (F) models [57]. For each of these models, we consider an additional variation accounting for the WR star tidal spin-up mechanism described by Bavera et al. (2020, [56]). Also, we account for spin tilts induced by core-collapse supernova explosions.

We selected these cases because they encompass the differences in current astrophysical models, ranging from very effective (F) to highly inefficient angular momentum transport (G). We compare them agnostically, as toy models, without focusing on their astrophysical features.

This paper is organized as follows. Section 2 presents our population-synthesis models. Section 3 describes the hierarchical Bayesian framework we used and discusses the LVK events used in our study. We lay down the results in Section 4 and summarize our conclusions in Section 5.

2. Models

2.1. MOBSE *and Natal Kicks*

We simulated our binary systems with the code MOBSE [95,96]. MOBSE is a custom and upgraded version of BSE [97,98], in which we introduced metallicity-dependent stellar winds for OB [99], WR [49], and luminous blue variable stars [100]. MOBSE includes a formalism for electron-capture [101], core-collapse [102], and (pulsational) pair-instability supernovae [103]. Here, we adopt the rapid core-collapse supernova prescription, which enforces a gap between the maximum mass of neutron stars and the minimum mass of BHs (2–5 $M_\odot$) [104,105]. Appendix A shows our results for the delayed core-collapse supernova model [102], which instead predicts a smooth transition between the maximum mass of a neutron star and the minimum BH mass.

Considering that there are still large uncertainties about natal kicks, e.g., [102,106,107], we decided to compare the following three models because they encompass the main uncertainties and are simple enough (1–3 free parameters) to allow us to easily interpret the results:

- A unified kick model, in which both neutron stars and BHs receive a kick $v_{\rm kick} \propto m_{\rm ej}/m_{\rm rem}$, where $m_{\rm ej}$ is the mass of the ejecta and $m_{\rm rem}$ the mass of the compact remnant [108, hereafter GM20]. This model naturally produces low kicks for electron-capture, stripped, and ultrastripped supernovae [109,110]. This model is similar to the one presented by Bray and Eldridge [106] and Bray and Eldridge [107]. It is also analogous to the model by Fryer et al. [102] but with a relevant difference: GM20 normalizes the kick by the BH mass, while Fryer et al. [102] normalize it by the total final mass of the star. Hereafter, we call this model GM20.
- A model in which compact-object kicks are drawn from a Maxwellian curve with one-dimensional root-mean-square $\sigma = 265$ km s^{-1}, consistent with observations of galactic pulsars [111]. This can be considered as an upper limit for BH natal kicks, because we assume that the natal kick distribution is the same for neutron stars and BHs, regardless of the larger BH mass. Hereafter, we name this model σ265.
- A model in which compact-object kicks are drawn from a Maxwellian curve with $\sigma = 150$ km s^{-1}. This value of σ is more similar to what is suggested from indirect measurements of galactic BH kicks [e.g., 112,113]. Hereafter, we refer to this model as σ150.

We show the three models in Figure 1. The peak at zero kick in the PDF for model GM20 corresponds to BHs born from a direct collapse (i.e., with no ejected mass $m_{\rm ej} = 0$).

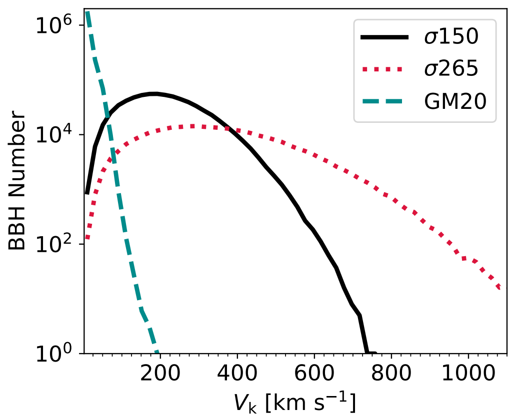

Figure 1. Distribution of kick magnitudes $V_{\rm k}$ of the simulated BBH mergers. We show the kick magnitude of both the first- and second-born BHs for each BBH. Dashed dark-cyan line: model GM20; solid black line: σ150; dotted red line: σ265. This figure only shows the kick magnitude of BHs that merge within the lifetime of the Universe in our MOBSE catalogues. Different metallicities are weighted equally.

For more details about MOBSE, see [100]. MOBSE is an open-source code and can be downloaded from https://gitlab.com/micmap/mobse_open (accessed on 4 September 2023).

2.2. Spin Magnitude

We implemented four models for the spin magnitude in MOBSE, the first three from Belczynski et al. (2020, [57]) and the fourth from Bouffanais et al. (2019, [33]). Given the large uncertainties on angular momentum transport, we do not claim that these four models are a complete description of the underlying physics: our models must be regarded as toy models, which encompass current uncertainties on BH spin magnitudes.

2.2.1. Geneva (G) Model

In the Geneva (hereafter, G) model, the dimensionless natal spin magnitude of a BH (χ) can be approximated as:

$$\chi = \begin{cases} 0.85 & M_{\rm CO} \leq m_1 \\ a\, M_{\rm CO} + b & m_1 < M_{\rm CO} < m_2 \\ a_{\rm low} & M_{\rm CO}, \geq m_2 \end{cases} \tag{1}$$

where $a = -0.088$ for all models, $M_{\rm CO}$ is the final carbon–oxygen mass of the progenitor star, while the values of b, m_1, m_2, and $a_{\rm low}$ depend on metallicity, as indicated in Table 1. This model comes from a fit [57] to the Geneva evolutionary tracks described by Ekström et al. [77], in which angular momentum transport is relatively inefficient.

Table 1. Parameters adopted in model G. See Equation (1) for details.

b	m_1 ($M_\odot$)	m_2 ($M_\odot$)	$a_{\rm low}$	Z
2.258	16.0	24.2	0.13	≥ 0.010
3.578	31.0	37.8	0.25	$[0.004, 0.010)$
2.434	18.0	27.7	0.0	$[0.0012, 0.004)$
3.666	32.0	38.8	0.25	< 0.0012

2.2.2. MESA (M) Model

In the M model, we use the fits done by Belczynski et al. (2020, [57]) to a set of stellar tracks run with the MESA code. MESA models the transport of angular momentum according to the Tayler–Spruit magnetic dynamo (Spruit et al. [80], see also Cantiello et al. [74]). This yields a dimensionless natal BH spin

$$\chi = \begin{cases} a_1\, M_{\rm CO} + b_1 & \text{if } M_{\rm CO} \leq m_1 \\ a_2\, M_{\rm CO} + b_2 & \text{if } M_{\rm CO} > m_1, \end{cases} \tag{2}$$

where a_1, b_1, and m_1 are given in Table 2.

Table 2. Parameters adopted in model M. See Equation (2) for details.

a_1	b_1	a_2	b_2	m_1 ($M_\odot$)	Z
-0.0016	0.115	-	-	∞	≥ 0.010
-0.0006	0.105	-	-	∞	$[0.004, 0.010)$
0.0076	0.050	-0.0019	0.165	12.09	$[0.0012, 0.004)$
-0.0010	0.125	-	-	∞	≤ 0.0012

2.2.3. Fuller (F) Model

Fuller et al. (2019, [70]) predict that angular momentum transport can be even more efficient than the one predicted by the Tayler–Spruit dynamo. Belczynski et al. (2020, [57]) summarize the results of the model by Fuller et al. (2019, [70]) simply as $\chi = 0.01$ for all single stars and metallicities.

2.2.4. Maxwellian Model (Max)

Finally, we also introduce a toy model in which we represent the spin of a BH as a random number drawn from a Maxwellian curve with one-dimensional root-mean-square $\sigma_\chi = 0.1$ and truncated to $\chi_{\rm max} = 1.0$. This model [33] is a good match to the distribution arising from LVK data, e.g., [3,4,7]. Hereafter, we indicate this Maxwellian toy model as Max, for brevity.

2.3. Tidal Spin-Up

The progenitor star of the second-born BH can be substantially spun up by tidal interactions, as we expect from the fundamentals of tidal evolution theory [97,114]. In the scenario explored by Bavera et al. (2020, [56]), a common-envelope or an efficient stable mass transfer episode can lead to the formation of a BH–WR binary system, in which the WR star is the result of mass stripping. The orbital period of this BH–WR binary system can be sufficiently short to lead to efficient tidal synchronisation and spin–orbit coupling. The WR star is then efficiently spun up. If the WR star then collapses to a BH directly, the final spin of the BH will retain the imprint of the final WR spin.

Bavera et al. (2021, [115]) derive a fitting formula to describe the spin-up of the WR star and the final spin of the second-born BH:

$$\chi = \begin{cases} \alpha_{\rm WR} \log^2_{10}\left(P/[\rm day]\right) + \beta_{\rm WR}\, \log_{10}\left(P/\rm day\right) & {\rm if} P \leq 1\,{\rm d} \\ 0 & \text{otherwise,} \end{cases} \tag{3}$$

where P is the orbital period of the BH–WR system, $\alpha_{\rm WR} = f\left(M_{\rm WR}, c_1^\alpha, c_2^\alpha, c_3^\alpha\right)$ and $\beta_{\rm WR} = f\left(M_{WR}, c_1^\beta, c_2^\beta, c_3^\beta\right)$. In this definition,

$$f(M_{\rm WR}, c_1, c_2, c_3) = \frac{-c_1}{c_2 + \exp\left(-c_3 M_{\rm WR}/[{\rm M}_\odot]\right)}, \tag{4}$$

where $M_{\rm WR}$ is the mass of the WR star, while the coefficients c_1, c_2, and c_3 are determined through nonlinear least-square minimization and can be found in [115]. These fitting formulas were derived assuming the delayed model for a core-collapse supernova [102]. In Appendix A, we compare the results of the delayed and rapid supernova model and find negligible differences. Another important assumption of the model is that the common envelope ejection efficiency is $\alpha = 1$ (which is the same as we assume here). Different values for the common-envelope efficiency parameters and the natal kicks affect the results. Bavera et al. (2021, [115]) discuss these uncertainties in detail. In MOBSE, we can use these fits for the spin of the second-born BH, while still adopting one of the models presented in the previous subsections (G, M, F, and Max) for the first-born BH.

2.4. Spin Orientation

We assume that natal kicks are the only source of misalignment between the orbital angular momentum vector of the binary system and the direction of BH spins [23,92]. Furthermore, we conservatively assume that accretion onto the first-born BH cannot change the direction of its spin [116]. For simplicity, we also neglect the spin-flip process [93]. Under such assumptions, we can derive the angle between the direction of the spins of the two compact objects and that of the orbital angular momentum of the binary system as [21,23]

$$\cos\delta = \cos\left(\nu_1\right)\,\cos\left(\nu_2\right) + \sin\left(\nu_1\right)\,\sin\left(\nu_2\right)\,\cos\left(\phi\right), \tag{5}$$

where ν_i is the angle between the new ($\vec{L}_{\rm new}$) and the old ($\vec{L}_{\rm old}$) orbital angular momentum after a supernova ($i = 1, 2$ corresponding to the first and second supernova), so that

$\cos(\nu) = \vec{L}_{\rm new} \cdot \vec{L}_{\rm old}/(L_{\rm new}\, L_{\rm old})$, while ϕ is the phase of the projection of the orbital angular momentum into the orbital plane.

2.5. Setup of MOBSE Runs

Hereafter, we consider eight possible models for the spins (see also Table 3):

- The first four models (hereafter, G, M, F, and Max) adopt the Geneva, Mesa, Fuller, and Maxwellian models for both the first- and second-born BHs;
- The other four models (hereafter, G_B21, M_B21, F_B21, and Max_B21) adopt the fits by Bavera et al. (2021, [115]) for the second-born BH and the Geneva, Mesa, Fuller, and Maxwellian models for the first-born BH.

Table 3. Description of the runs performed for this work. [a] Model for the spin magnitude (Section 2.2). [b] Correction of the spin magnitude accounting for tidal spin-up, as described in B21 (Section 2.3). [c] Model for the natal kick (Section 2.1).

Model Name	Spin Magnitude [a]	B21 [b]	Kick Model [c]
G	Geneva (G)	no	GM20, σ265, σ150
G_B21	Geneva (G)	yes	GM20, σ265, σ150
M	MESA (M)	no	GM20, σ265, σ150
M_B21	MESA (M)	yes	GM20, σ265, σ150
F	Fuller (F)	no	GM20, σ265, σ150
F_B21	Fuller (F)	yes	GM20, σ265, σ150
Max	Maxwellian (Max)	no	GM20, σ265, σ150
Max_B21	Maxwellian (Max)	yes	GM20, σ265, σ150

The model by Bavera et al. [115] was derived assuming a very efficient angular momentum transport and simulating the binary evolution with MESA [117]. Hence, the fitting formula by Bavera et al. [115] can be naturally associated with models F and M, which are based on an efficient angular momentum transport. Here, we also coupled it with models Max (toy model) and G (inefficient angular momentum transport), because our purpose was to encompass all possible uncertainties and compare our models agnostically.

For each of the aforementioned eight spin models, we considered three different kick models: the GM20, σ265, and σ150 models discussed in Section 2.1.

Finally, for each of these 24 models, we considered 12 metallicities ($Z = 0.0002$, 0.0004, 0.0008, 0.0012, 0.0016, 0.002, 0.004, 0.006, 0.008, 0.012, 0.016, and 0.02). For each metallicity, we ran 10^7 (2×10^7) binary systems if $Z \leq 0.002$ ($Z \geq 0.004$). Hence, for each model we ran 1.8×10^8 binary systems, for a total of 4.32×10^9 binary systems encompassing the eight models.

We sampled the initial conditions for each binary system as follows. We randomly drew the zero-age main sequence mass of the primary stars from a Kroupa [118] initial mass function in the range $5 - 150$ $M_\odot$. The initial orbital parameters (semimajor axis, orbital eccentricity, and mass ratio) of binary stars were randomly drawn as already described in [119]. In particular, we derived the mass ratios $q \equiv m_2/m_1$ (with $m_2 \leq m_1$) as $\mathcal{F}(q) \propto q^{-0.1}$ with $q \in [0.1, 1]$, the orbital period P from $\mathcal{F}(\Pi) \propto\ -0.55$ with $\Pi = \log_{10}(P/\mathrm{d}) \in [0.15, 5.5]$, and the eccentricity e from $\mathcal{F}(e) \propto e^{-0.42}$ with $0 \leq e \leq 0.9$. These distributions resulted from fitting the observational data of massive binary systems in nearby young clusters [120].

As to the main binary evolution parameters, here, we used $\alpha = 1$ for the common envelope, while the parameter λ depended on the stellar structure as described in [121]. The other binary evolution parameters were set up as described in [119].

Each of the resulting eight MOBSE catalogues consisted of a number of BBH mergers ranging from 1.47×10^5 for the high-kick case (σ265) to 1.05×10^6 for the lowest-kick model (GM20). These numbers are sufficient to claim that differences in the kick (Figure 1) and mass (Figure 2) distributions are robust to stochastic fluctuations, as already discussed by Iorio et al. [122].

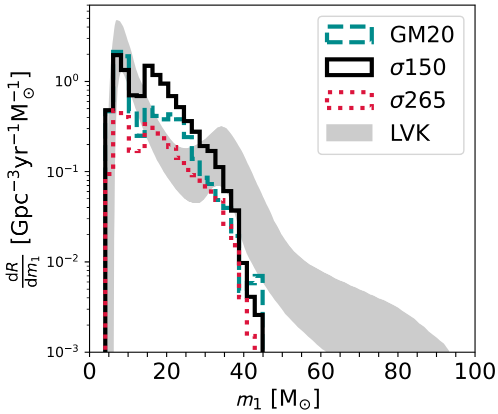

Figure 2. Distribution of the primary masses of M_B21 for each kick model: GM20 (dashed dark-cyan line), σ150 (solid black line), and σ265 (dotted red line). The shaded grey area is the distribution for the fiducial POWER LAW + PEAK model from the LVK collaboration [7].

2.6. Merger Rate Density

We estimated the evolution of BBH mergers with a redshift by using our semianalytic code COSMO$\mathcal{R}$ATE [119,123]. With COSMO$\mathcal{R}$ATE, we convolved our MOBSE catalogues (Section 2.5) with an observation-based metallicity-dependent star formation rate (SFR) density evolution of the Universe, SFRD(z, Z), in order to estimate the merger rate density of BBHs as

$$\mathcal{R}_{\rm BBH}(z) = \int_{z_{\rm max}}^{z} \left[\int_{Z_{\rm min}}^{Z_{\rm max}} {\rm SFRD}(z', Z)\, \mathcal{F}(z', z, Z)\, {\rm d}Z \right] \frac{{\rm d}t(z')}{{\rm d}z'}\, {\rm d}z', \tag{6}$$

where

$$\frac{{\rm d}t(z')}{{\rm d}z'} = [H_0\,(1+z')]^{-1}\,[(1+z')^3\Omega_M + \Omega_\Lambda]^{-1/2}. \tag{7}$$

In the above equation, H_0 is the Hubble constant, Ω_M and Ω_Λ are the matter and energy density, respectively. We adopted the values in [124]. The term $\mathcal{F}(z', z, Z)$ is given by:

$$\mathcal{F}(z', z, Z) = \frac{1}{\mathcal{M}_{\rm TOT}(Z)} \frac{{\rm d}\mathcal{N}(z', z, Z)}{{\rm d}t(z)}, \tag{8}$$

where $\mathcal{M}_{\rm TOT}(Z)$ is the total simulated initial stellar mass, and ${\rm d}\mathcal{N}(z', z, Z)/{\rm d}t(z)$ is the rate of BBHs forming from stars with initial metallicity Z at redshift z' and merging at z, extracted from our MOBSE catalogues. In COSMO$\mathcal{R}$ATE, SFRD(z, Z) is given by

$${\rm SFRD}(z', Z) = \psi(z')\, p(z', Z), \tag{9}$$

where $\psi(z')$ is the cosmic SFR density at formation redshift z', and $p(z', Z)$ is the log-normal distribution of metallicities Z at fixed formation redshift z', with average $\mu(z')$ and spread σ_Z. Here, we took both $\psi(z)$ and $\mu(z)$ from Madau and Fragos (2017, [125]). Finally, we assumed a metallicity spread $\sigma_Z = 0.3$.

2.7. Hyperparametric Model Description

For each of our models (Table 3), described by their hyperparameters λ, we predicted the distributions of BBH mergers

$$\frac{{\rm d}N}{{\rm d}\theta}(\lambda) = N_\lambda\, p(\theta|\lambda), \tag{10}$$

where θ are the merger parameters, and N_λ is the total number of mergers predicted by the model. Assuming an instrumental horizon redshift $z_{\rm max} = 1.5$, N_λ can be calculated as

$$N_\lambda = \int_0^{z_{\rm max}} \mathcal{R}(z)\, \frac{{\rm d}V_{\rm c}}{{\rm d}z}\, \frac{T_{\rm obs}}{(1+z)}\, {\rm d}z, \tag{11}$$

where $\frac{{\rm d}V_{\rm c}}{{\rm d}z}$ is the comoving volume and $T_{\rm obs}$ the observation duration.

To model the population of merging BBHs, we chose five observable parameters $\theta = \{\mathcal{M}_{\rm c}, q, z, \chi_{\rm eff}, \chi_{\rm p}\}$, where $\mathcal{M}_{\rm c} = (m_1\, m_2)^{3/5}/(m_1 + m_2)^{1/5}$ is the chirp mass in the source frame with m_1 (m_2) the masses of the primary (secondary) BH of the binary, $q = m_2/m_1$, and z is the redshift of the merger. In addition, we used two spin parameters: the effective spin ($\chi_{\rm eff}$) and the precessing spin ($\chi_{\rm p}$). The effective spin $\chi_{\rm eff}$ is the mass-weighted projection of the two individual BH spins on the binary orbital angular momentum $\vec{L}$

$$\chi_{\rm eff} = \frac{(\vec{\chi}_1 + q\,\vec{\chi}_2)}{1+q} \cdot \frac{\vec{L}}{L}, \tag{12}$$

where $\vec{\chi}_{1,2} = \vec{s}_{1,2}\, c/(G\, m_{1,2}^2)$ is the dimensionless spin parameter of the two BHs. The precessing spin $\chi_{\rm p}$ is defined as

$$\chi_{\rm p} = \max(\chi_{1,\perp},\, A\, \chi_{2,\perp}), \tag{13}$$

where $\chi_{1,\perp}$ ($\chi_{2,\perp}$) is the spin component of the primary (secondary) BH perpendicular to the orbital angular momentum vector $\vec{L}$, and $A = (4\,q + 3)\, q/(4 + 3\, q)$.

To compute the distributions $p(\theta|\lambda)$, we constructed a catalogue of 10^6 sources for all possible combinations of hyperparameters λ, using the merger rate density and the metallicity given by COSMO$\mathcal{R}$ATE. From these catalogues, we derived continuous estimations of $p(\theta|\lambda)$ by making use of a Gaussian kernel density estimation assuming a bandwidth of 0.15.

3. Hierarchical Bayesian Inference

The likelihood associated to an astrophysical model, given a dataset $\mathcal{H} = \{h^k\}_{k=1}^{N_{\rm obs}}$ of $N_{\rm obs}$ GW observations, can be written as, e.g., [33–35,126–128]:

$$\mathcal{L}(\lambda|\mathcal{H}) = \prod_{k=1}^{N_{\rm obs}} \frac{\mathcal{I}^k}{\beta(\lambda)}, \tag{14}$$

where $N_{\rm obs}$ is the number of events observed by the LVK, with an ensemble of parameters θ, $\mathcal{I}^k$ is the match of the k^{th} event with the model λ and $\beta(\lambda)$ the detection efficiency associated to the model. The detection efficiency of a model λ is defined as the ratio of the number of eventually detected mergers μ_λ over all the mergers predicted by this model N_λ and can be expressed as:

$$\beta(\lambda) = \frac{\mu_\lambda}{N_\lambda} = \int_\theta p(\theta|\lambda)\, p_{\rm det}(\theta)\, {\rm d}\theta, \tag{15}$$

where $p_{\rm det}(\theta)$ is the detection probability for a set of parameters θ.

Finally, $\mathcal{I}^k$ is the integral of an event's log-likelihood derived from posteriors and priors from data samples released by the LVK collaboration. It is approximated with a Monte Carlo approach as:

$$\mathcal{I}^k = \int \mathcal{L}^k(h^k|\theta)\, p(\theta|\lambda)\, {\rm d}\theta \approx \frac{1}{N_s^k} \sum_{i=1}^{N_s^k} \frac{p(\theta_i^k|\lambda)}{\pi^k(\theta_i^k)}, \tag{16}$$

where θ_i^k is the i^{th} posterior sample of the k^{th} detection and N_s^k is the total number of posterior samples for the k^{th} detection. To compute the prior term in the denominator, we also used a Gaussian kernel density estimation.

The standard model comparison used to compute the Bayes factors B between two models λ_i and λ_j is defined by the ratio of posteriors:

$$B = \frac{p(\lambda_i|\mathcal{H})}{p(\lambda_j|\mathcal{H})}. \tag{17}$$

In practice, we assumed the same prior for all models in order to avoid any preference for any models. Therefore, the Bayes factor expression simplified as:

$$B = \frac{\mathcal{L}(\lambda_i|\mathcal{H})}{\mathcal{L}(\lambda_j|\mathcal{H})}. \tag{18}$$

We adopted the formalism described in Equations (14)–(18) to perform a hierarchical Bayesian inference to compare the astrophysical models presented in Section 2 with the third gravitational-wave transient catalogue (GWTC-3, [6,7]). GWTC-3 contains 90 event candidates with a probability of astrophysical origin $p_{\text{astro}} > 0.5$. From GWTC-3, we extracted 59 confident detections of BBHs with a false alarm rate FAR < 0.25 yr^{-1}. In this subsample, we did not include binary neutron stars and neutron star–BH systems, and we also excluded the other BBH candidates with a higher FAR. Our chosen FAR threshold ensured a sufficiently pure sample for our analysis [7]. A list of the events used in this study is available in Appendix C. For the observable parameters θ, we used the choice described in Section 2.7, namely, $\theta = \{\mathcal{M}_c, q, z, \chi_{\text{eff}}, \chi_p\}$.

4. Results

4.1. Masses

The primary BH mass (Figure 2) and mass ratio distributions (Figure 3) do not depend on the spin model, by construction. Therefore, we only show different natal kicks models in these figures. Models $\sigma 150$ and $\sigma 265$ show a similar distribution of primary masses with two peaks of similar importance, one at $m_1 \approx 8$ M$_\odot$ and the other (broader) peak at $m_1 \approx 18$ M$_\odot$. In contrast, model GM20 has a dominant peak at $m_1 \approx 8$ M$_\odot$. The main reason for this difference is that the natal kick is independent of both BH mass and ejected mass in both models $\sigma 150$ and $\sigma 265$ [122]. Hence, binaries hosting low-mass BHs break up more easily during a supernova explosion in models $\sigma 150$ and $\sigma 265$ compared to model GM20. In contrast, most BHs receive low natal kicks in model GM20, and their binaries do not break.

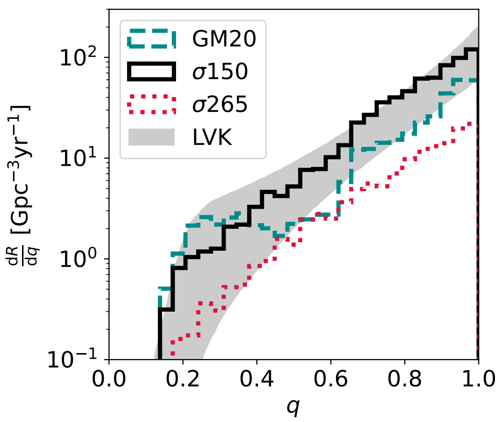

Figure 3. Distribution of the mass ratios of M_B21 for each kick model: GM20 (dashed dark-cyan line), $\sigma 150$ (solid black line), and $\sigma 265$ (dotted red line). The shaded grey area is the distribution for the fiducial POWER LAW + PEAK model from the LVK collaboration [7].

Figures 2 and 3 also compare the distribution of our models with the distributions inferred by LVK detections adopting the POWER LAW + PEAK parametric model [7]. The models present a significant excess in the range $m_1 \approx 15 - 25$ M$_\odot$ to the data. Finally, the peak at $m_1 \approx 9$ M$_\odot$ in the data approximately matches the peak at $m1 \approx 8$ M$_\odot$ in the models. The main features of our population synthesis models (in particular, the peaks at $m_1 \approx 8 - 10$ M$_\odot$ and $m_1 \approx 15 - 20$ M$_\odot$) are also common to other population-synthesis models, e.g., [57,63], and mostly stem from the core-collapse SN prescriptions by [102]. The features of these models fall outside the 90% credible region for the primary BH mass with respect to the POWER LAW + PEAK model shown in Figure 2. The difference is particularly evident for $m_1 \approx 15 - 20$ M$_\odot$ and for the high-mass tail. Alternative core-collapse SN models, e.g., [59,61,103,122,129,130], produce different features and deserve further investigation. Furthermore, here, we did not consider the dynamical formation channels in star clusters and AGN discs, which can significantly affect the mass distribution and add several degrees of freedom to this issue [23,43,131–133].

4.2. Spin Parameters

Figure 4 shows the distribution of spin parameters $\chi_{\rm p}$ and $\chi_{\rm eff}$ for all of our models. By construction, large spins are much more common in models G and G_B21, while models F and F_B21 have a strong predominance of vanishingly small spins. Models M, M_B21, Max, and Max_B21 are intermediate between the other two extreme models. Including or not the correction by B21 has a negligible impact on the distribution of $\chi_{\rm p}$ and $\chi_{\rm eff}$ for models G, because of the predominance of large spin magnitudes. In contrast, introducing the spin-up correction by B21 has a key impact on models F, because it is the only way to account for mild to large spins in these models. The correction by B21 is important also for models M and Max, being responsible for the large-spin wings.

Finally, our model with slow kicks (GM20) results in a distribution of $\chi_{\rm p}$ that is more peaked at zero (for models G, M, and Max) with respect to the other two kick models (σ150 and σ265). In fact, the supernova kicks in model GM20 are not large enough to appreciably misalign BH spins (see Figure 1). A similar effect is visible in the distribution of $\chi_{\rm eff}$: model σ265 produces a distribution of $\chi_{\rm eff}$ that is less asymmetric about the zero with respect to models σ150 and especially GM20.

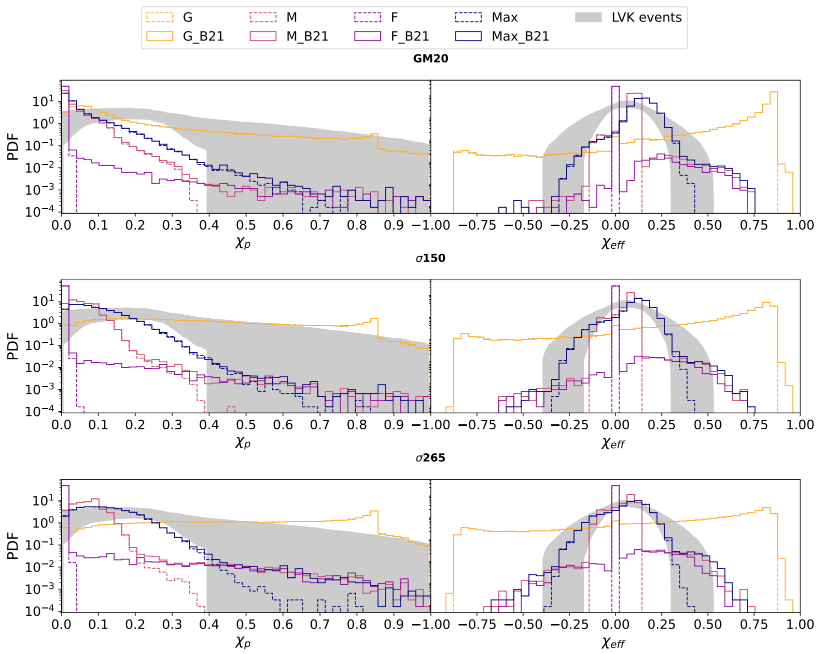

Figure 4. Distribution of $\chi_{\rm p}$ (left) and $\chi_{\rm eff}$ (right) for all of our models. Different colours refer to the spin model: G, M, F, and Max. Solid (dashed) lines include (do not include) the tidal spin-up

model by B21. From top to bottom: GM20, σ150, and σ265. The shaded grey area shows the inferred distribution from the LVK collaboration [7].

4.3. Model Selection

Figure 5 and Table 4 report the values of the log-likelihood $\log \mathcal{L}$ defined in Equation (14). The purpose of the log-likelihood values is just to compare models to each other: they do not tell us if a model is a good match to the data in the absolute sense. Therefore, we can quantify the difference between two models A and B by computing the average absolute difference in percentage

$$\Delta\log\mathcal{L}(\mathrm{A},\,\mathrm{B}) = \left\langle \frac{2\left|\log\mathcal{L}^{\mathrm{A}} - \log\mathcal{L}^{\mathrm{B}}\right|}{\log\mathcal{L}^{\mathrm{A}} + \log\mathcal{L}^{\mathrm{B}}} \right\rangle_{var}, \tag{19}$$

on the non-A, B variation *var* (*var* would be a kick (spin) if A and B are spin (kick) models). For example to compare the two models G and G_B21, A and B become G_B21 and G, and $var = \{\mathrm{GM20},\, \sigma150,\, \sigma265\}$.

The tidal spin-up mechanism (B21) affects the spin of a small part of the population of each model (Figure 4). However, it improves the likelihood of the F and M models significantly (e.g., $\Delta\log\mathcal{L}(\mathrm{M\_B21},\, \mathrm{M}) = 89\%$, Table 4). This improvement of the log-likelihood can be explained by the presence of higher values of χ_p and χ_eff in the distribution of populations M_B21 and F_B21 compared to M and F (Figure 4).

Model F yields $\mathcal{L}(\mathrm{F}) = -\infty$, because the LVK data have support for non vanishingly small spins, i.e., outside the values permitted by model F ($|\chi_\mathrm{eff}| > 0.05$). However, it is sufficient to inject a tiny subpopulation of spinning BHs, by switching on the B21 correction, and the F model becomes one of the best considered models. In fact, the F_B21 model only includes 0.4% of BHs with $\chi > 0.01$ and achieves $\log \mathcal{L} > 200$ (for kick models σ150 and σ265).

Table 4. Log-likelihood $\mathcal{L}$ (Equation (18)) estimated with five merger parameters $\theta = \{\mathcal{M}_\mathrm{c}, z, \chi_\mathrm{eff}, q, \chi_\mathrm{p}\}$.

Model Name	GM20	σ150	σ265
G	−1	149	145
G_B21	−12	150	141
M	0	162	171
M_B21	36	232	232
F	$-\infty$	$-\infty$	$-\infty$
F_B21	88	250	242
Max	92	255	254
Max_B21	106	257	250

The G and G_B21 spin models exhibit lower log-likelihood values than the others for all kick models: $\log\mathcal{L} \leqslant 150$ for σ150 and σ265, and $\log\mathcal{L} < 0$ for GM20. This happens because the LVK data have little support for extreme values $\chi_\mathrm{eff} < -0.5$ and $\chi_\mathrm{eff} > 0.5$ (Figure 4).

The kick models σ150 and σ265 show similar results ($\Delta\log\mathcal{L}(\sigma150, \sigma265) < 3\%$) for every spin assumptions. Also, for all spin assumptions, the GM20 kick model scores a significantly lower likelihood than the other models σ150 and σ265 with $\Delta\log\mathcal{L}(\sigma150, \mathrm{GM20}) \sim \Delta\log\mathcal{L}(\sigma265, GM20) \sim 150\%$. This result can be explained by the high peak of model GM20 at low chirp masses ($\mathcal{M}_\mathrm{c} \sim 8\ \mathrm{M}_\odot$, see Section 4.1 and Figure 2) and by the low value of χ_p compared to the other kick models (Figure 4).

Models Max and Max_B21 are possibly the best match to the data, but this is not surprising, because they were built as a toy model to visually match the data. Among the astrophysically motivated models (i.e., after excluding the Max model), M, M_B21, and F_B21 (with kick models σ150 and σ265) are the most favoured by the data. This might be interpreted as a support for the Tayler–Spruit instability mechanism (adopted in models M) and for the tidal spin-up model by B21.

4.4. Importance of χ_p

The χ_p parameter encodes information on the spin component in the orbital plane. Its impact on gravitational-wave signals is much lower than that of χ_eff, and therefore, its measurement is less precise. To understand the impact of χ_p on our results, we reran the analysis without this parameter. The results are shown in Table 5 and in Figure 5 with empty markers. Figure 5 shows that if we do not include χ_p, the models M and M_B21 have almost the same log-likelihood, and even the F model yields a positive log-likelihood. Furthermore, the analysis without χ_p results in significantly larger values of $\mathcal{L}$ for the kick model GM20. Our results demonstrate that the measured χ_p of GWTC-3 BBHs carries substantial information, despite the large uncertainties.

Table 5. Log-likelihood $\mathcal{L}$ (Equation (18)) estimated with four merger parameters $\theta = \{\mathcal{M}_\mathrm{c}, z, \chi_\mathrm{eff}, q\}$. Here, we ignore χ_p.

Model Name	GM20	σ150	σ265
G	35	146	147
G_B21	47	149	154
M	141	192	190
M_B21	130	199	180
F	85	146	138
F_B21	185	207	180
Max	161	208	155
Max_B21	160	206	200

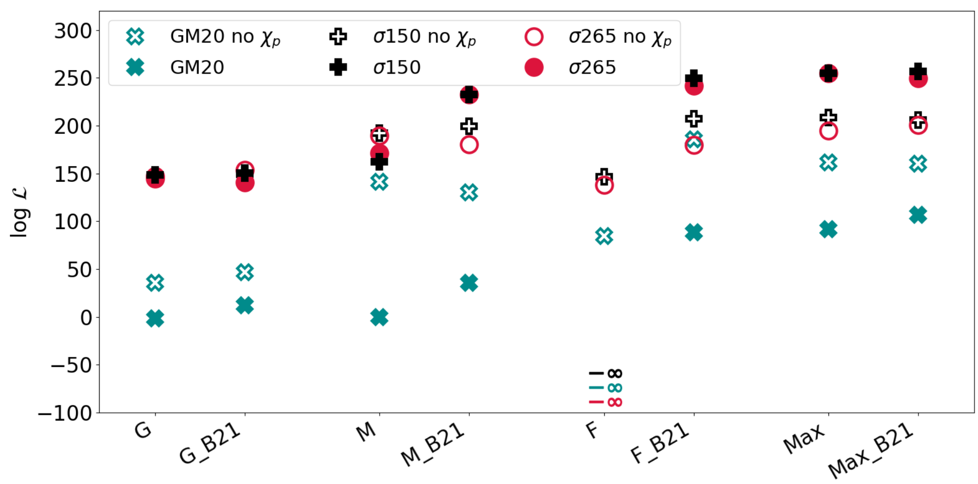

Figure 5. Values of the log-likelihood $\mathcal{L}$ defined in Equation (18) for the four different models Geneva (G), MESA (M), Fuller (F), and Maxwellian (Max), with/without the tidal spin-up mechanism (B21). Blue crosses: GM20; dark pluses: σ150; red circles: σ265.

5. Discussion

The spin magnitude of BHs is largely uncertain, mostly because we do not fully understand angular momentum transport in massive stars. In order to encompass the main uncertainties, we took a number of toy models for the BH spin, implemented them into our population-synthesis code MOBSE, and compared them against GWTC-3 data within a hierarchical Bayesian framework.

The data did not support models in which the entire BH population had vanishingly small spins (model F). This result was mainly driven by the χ_p parameter. This is in agreement with, e.g., the complementary analysis presented in [20]. They employed a variety of complementary methods to measure the distribution of spin magnitudes and orientations of BBH mergers and concluded that the existence of a subpopulation of BHs with vanishing spins was not required by the current data. Ref. [20] found that the fraction of nonspinning BHs could comprise up to ∼60–70% of the total population. In our F_B21 models, we had ∼99.6% of BHs with $\chi < 0.01$.

Other authors [134–137] recently claimed the existence of a subpopulation of zero-spin BHs. From our analysis, we cannot exclude the existence of such subpopulation, as the F model with B21 correction (F_B21) still represented a good match of the data. We found that models with large spins (G, G_B21) were less favoured by the data, but they were still acceptable if we allowed for large kicks.

Overall, we found a preference for large natal kicks. This result goes into the same direction as the work by Callister et al. 2021, [18]. Actually, this preference for large natal kicks is degenerate with the adopted formation channel. Had we included the dynamical formation channel in dense star clusters, we would have added a subpopulation of isotropically oriented spins (see, e.g., Figure 8 of Mapelli et al. [42]). In a forthcoming study, we will extend our analysis to a multichannel analysis. While it is unlikely that BBH mergers only originate from one single channel, adding more formation channels to a hierarchical Bayesian analysis dramatically increases the number of parameters, making it more difficult to reject some portions of the parameter space. Finally, some of our results depend on the usage of the MOBSE population-synthesis models. This mostly affects BBH masses, which depend on the assumptions on stellar tracks, binary evolution (e.g., the parameter of common-envelope efficiency), core-collapse supernovae (see, e.g., the comparison between rapid and delayed supernova model in Appendix A), and natal kicks. We refer to Iorio et al. [122] for a detailed comparison of various population-synthesis models. On the other hand, our main result, i.e., the poor performance of model F when χ_p was included in our hierarchical analysis, is robust with respect to such model assumptions. In fact, the estimated log-likelihood of model F ($\mathcal{L} = -\infty$, Table 4) did not change when we considered different kick models, even if these significantly affected the mass distribution. Our result confirms that not all LVK BBHs have vanishingly small spins.

6. Summary

The origin of BH spins is still controversial, and angular momentum transport inside massive stars is one of the main sources of uncertainty. Here, we applied hierarchical Bayesian inference to derive constraints on spin models from the 59 most confident BBH merger events in GWTC-3. We considered five parameters: chirp mass, mass ratio, redshift, effective spin, and precessing spin.

For the model selection, we used a set of binary population-synthesis simulations spanning different assumptions for BH spins and natal kicks. In particular, our spin models accounted for relatively inefficient (G), efficient (Max and M), and very efficient angular-momentum transport (F). A higher efficiency of angular momentum transport was associated with lower BH spins. In particular, model F predicted vanishingly small spins for the entire BH population. For each of our models, we also included the possibility that some BHs were tidally spun up (B21). These assumptions should be regarded as toy models, encompassing the main uncertainties on BH spin magnitude.

We also considered three different natal kick models: according to models σ265 and σ150, we randomly drew the kicks from a Maxwellian curve with $\sigma = 265$ and 150 km s^{-1}, respectively; in the third model (G20), we also derived the kicks from a Maxwellian curve with $\sigma = 265$ km s^{-1}, but the kick magnitude was then modulated by the ratio between the mass of the ejecta and the mass of the BH.

We summarize our main results as follows.

- Data from GWTC-3 do not support models in which the entire BH population has vanishingly small spins (model F).

- In contrast, models in which most spins are vanishingly small but that also include a subpopulation of tidally spun-up BHs (model F_B21) are a good match to the data.
- The models in which angular momentum transport is relatively inefficient (G and G_21) yield log-likelihood values that are lower than models with efficient angular momentum transport (M, M_B21, Max, and Max_B21).
- Models with large BH kicks (σ150 and σ265) are favoured by our analysis with respect to low-kick models (G20).
- Our results show that the precessing spin parameter $\chi_{\rm p}$ plays a crucial role in constraining the spin distribution of BBH mergers.

Author Contributions: Conceptualization, M.M.; Methodology, C.P., M.M. and Y.B.; Software, C.P. and Y.B.; Validation, F.S.; Formal analysis, C.P.; Investigation, R.R.; Resources, M.M.; Writing–original draft, C.P. and M.M.; Writing–review & editing, C.P. and M.M.; Supervision, M.M.; Funding acquisition, M.M. All authors have read and agreed to the published version of the manuscript.

Funding: This research was funded by the European Research Council for the ERC Consolidator grant DEMOBLACK, under contract No. 770017.

Data Availability Statement: The data underlying this article will be shared on reasonable request to the corresponding author. The latest public version of MOBSE can be downloaded from https://gitlab.com/micmap/mobse_open (accessed on 4 September 2023). COSMO$\mathcal{R}$ATE can be downloaded from https://gitlab.com/Filippo.santoliquido/cosmo_rate_public (accessed on 4 September 2023).

Acknowledgments: This research has made use of data or software obtained from the Gravitational Wave Open Science Center (gwosc.org, accessed on 4 September 2023), a service of LIGO Laboratory, the LIGO Scientific Collaboration, the Virgo Collaboration, and KAGRA. LIGO Laboratory and Advanced LIGO are funded by the United States National Science Foundation (NSF) as well as the Science and Technology Facilities Council (STFC) of the United Kingdom, the Max-Planck-Society (MPS), and the State of Niedersachsen/Germany for support of the construction of Advanced LIGO and construction and operation of the GEO600 detector. Additional support for Advanced LIGO was provided by the Australian Research Council. Virgo is funded through the European Gravitational Observatory (EGO), by the French Centre National de Recherche Scientifique (CNRS), the Italian Istituto Nazionale di Fisica Nucleare (INFN), and the Dutch Nikhef, with contributions by institutions from Belgium, Germany, Greece, Hungary, Ireland, Japan, Monaco, Poland, Portugal, and Spain. KAGRA is supported by the Ministry of Education, Culture, Sports, Science and Technology (MEXT), the Japan Society for the Promotion of Science (JSPS) in Japan, the National Research Foundation (NRF) and Ministry of Science and ICT (MSIT) in Korea, and the Academia Sinica (AS) and National Science and Technology Council (NSTC) in Taiwan [138,139]. This research made use of NUMPY [140] and SCIPY [141]. For the plots, we used MATPLOTLIB [142].

Conflicts of Interest: The authors declare no conflict of interest.

Appendix A. Delayed Model for Core-Collapse Supernovae

Here, we assume the delayed core-collapse supernova model for the BH mass, while in the main text we adopted the rapid supernova model. Both models are thoroughly described by Fryer et al. [102]. The delayed model predicts a smooth transition between the maximum neutron star mass and the minimum BH mass, while the rapid model enforces a mass gap. Bavera et al. [115] derived their fits adopting the delayed supernova model. Figure A1 shows the distribution of chirp mass $\mathcal{M}_{\rm c}$, effective spin $\chi_{\rm eff}$, precession spin $\chi_{\rm p}$, and mass ratio q for the delayed MESA model (hereafter, MD) and for the delayed MESA model with the Bavera et al. correction (hereafter, MD_B21) and compares them to models M and M_B21. We conclude that the choice of the rapid versus delayed model does not significantly impact the BBH parameters. The main difference is that the delayed model extends to lower chirp masses and does not show a sharp peak at $\mathcal{M}_{\rm c} = 8\ {\rm M}_\odot$, by construction.

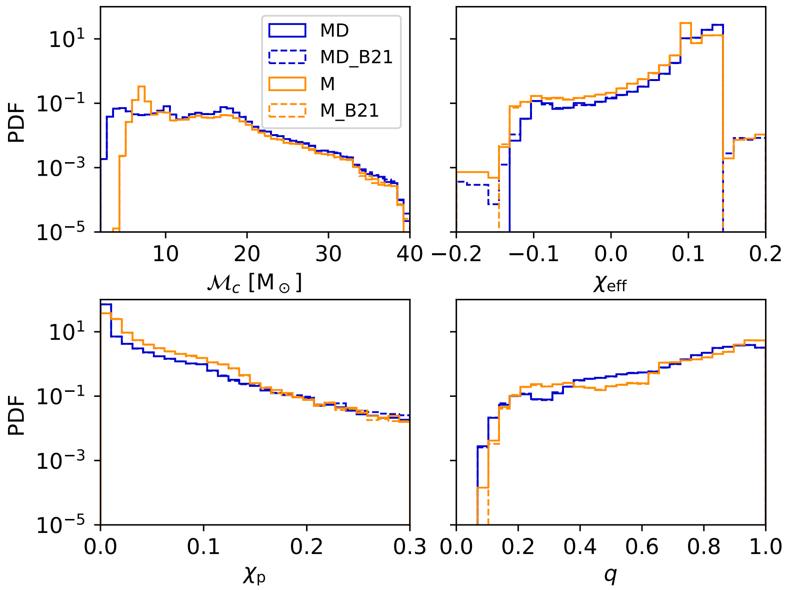

Figure A1. Probability density distribution (PDF) of chirp mass $\mathcal{M}_c$, effective spin $\chi_{\rm eff}$, precession spin $\chi_{\rm p}$, and mass ratio q for models M, M_B21, MD (MESA delayed), and MD_B21.

Appendix B. The Relation between χ and $m_{\rm CO}$ in Our Models

Figures A2–A4 show the BH spins (χ) versus the carbon–oxygen (CO) core mass of our population-synthesis catalogues and for the three kick models. In these figures, we show all the primary and secondary BHs together (not only BBH mergers). The comparison between the left-hand and right-hand plots shows the impact of the B21 correction for the tidal spin-up, and its dependence on the CO core mass.

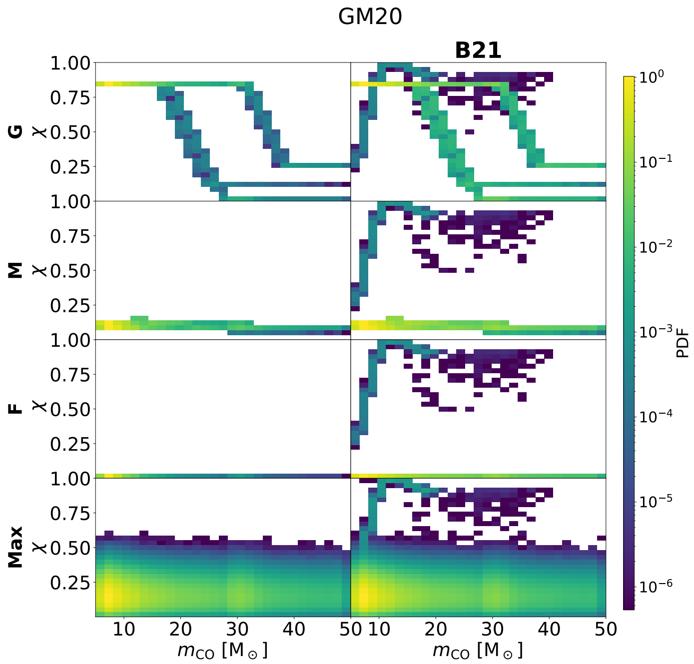

Figure A2. Two-dimensional histograms of the dimensionless spin magnitude χ versus the carbon–oxygen core mass of the progenitor star $m_{\rm CO}$ for all BHs (we plot primary and secondary BHs together) generated in our MOBSE simulations. We show the natal kick model *GM*20. The left-hand (right-hand) column shows the distribution for populations generated without (with) the B_21 formalism. From top to bottom: models G, M, F, and Max, respectively. We weighed each metallicity equally.

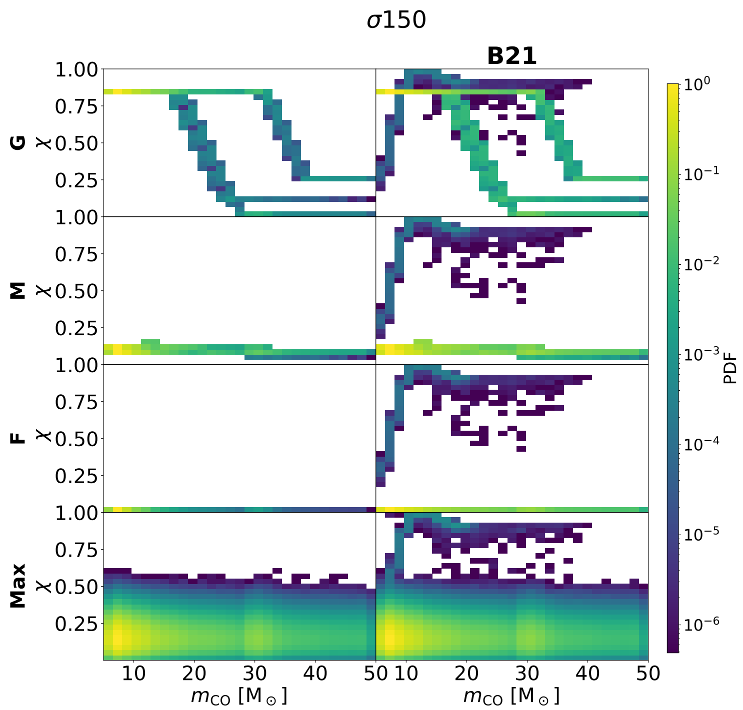

Figure A3. Same as Figure A2 but for the natal kick model σ150.

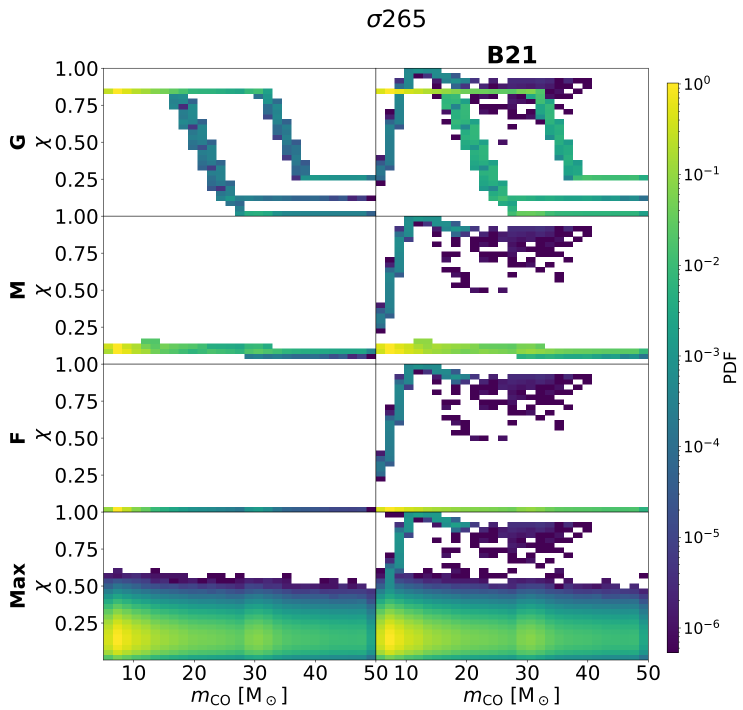

Figure A4. Same as Figure A2 but for the natal kick model σ265.

Appendix C. Sample of Gravitational-Wave Events

Table A1 lists all the possible BBHs (i.e., $m_2 > 2.5\mathrm{M}_\odot$) gravitational-wave event candidates we used in our study. From GWTC-3, we selected all the event candidates with $p_{\rm astro} > 0.9$ and FAR$< 0.25\ \mathrm{yr}^{-1}$, excluding the following systems:

- The (possible) neutron star–BH binary system GW190814;

- The BBH GW190521 ($m_1 = 98.4^{+33.6}_{-21.7} M_\odot$, $m_2 = 57.2^{+27.1}_{-30.1} M_\odot$ Abbott et al. [6]), which can form only via dynamical interactions according to our models, e.g., [41,131,132]. This last event is so unlikely in our population-synthesis model that it pulls down the values of all the likelihoods making the comparison between models difficult to perform. Figure A5 shows $\mathcal{I}^k$ for all events including GW190521, illustrating the gap in the match values.

Figure A5 shows the match values $\mathcal{I}$ as defined in Equation (16).

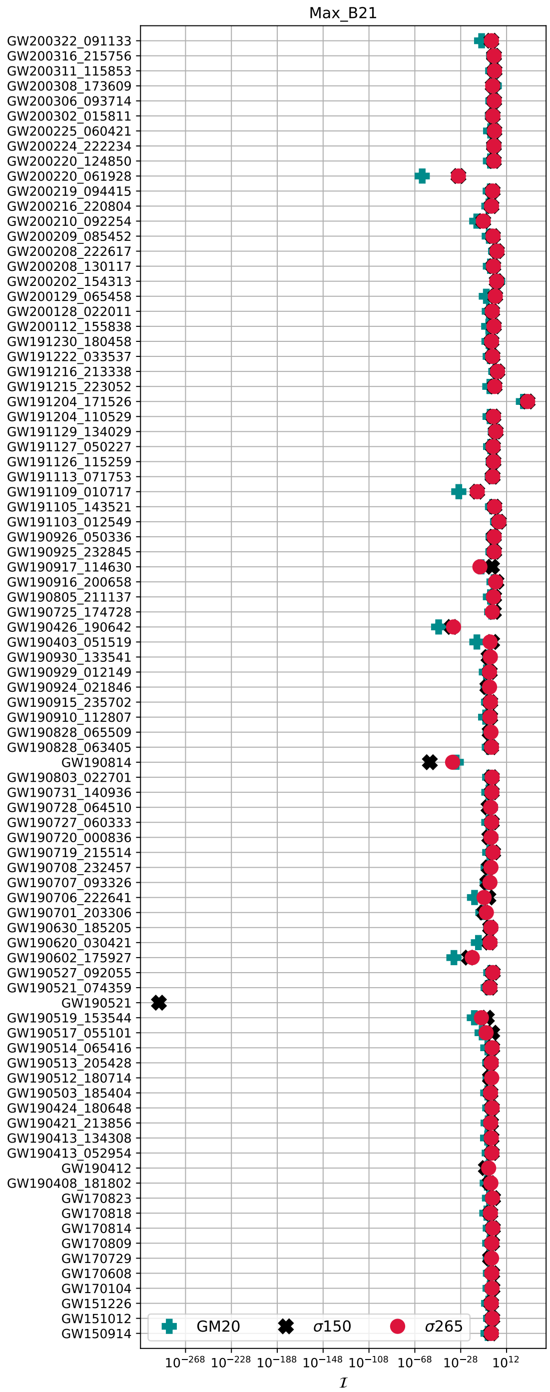

Figure A5. Values of the match of all events recorded as possible BBHs (i.e., $m_2 > 2.5 M_\odot$) by LVK for the spin model Max_B21 and for the three kick models. The missing points are null (i.e., $\mathcal{I}(\mathrm{GW190521}^{\mathrm{GM20}}) = \mathcal{I}(\mathrm{GW190521}^{\sigma_{265}}) = 0$.

Table A1. Catalogue of BBH events adopted in this study. The uncertainties shown stand for the 90% credible intervals.

Name	$\mathcal{M}_c(M_\odot)$	q	$\chi_{\rm eff}$	$\chi_{\rm p}$	z
GW150914	$28.6^{+1.7}_{-1.5}$	$0.86^{+0.12}_{-0.2}$	$-0.01^{+0.12}_{-0.13}$	$0.34^{+0.45}_{-0.25}$	$0.09^{+0.03}_{-0.03}$
GW151012	$15.2^{+2.1}_{-1.2}$	$0.59^{+0.36}_{-0.35}$	$0.05^{+0.31}_{-0.2}$	$0.33^{+0.45}_{-0.25}$	$0.21^{+0.09}_{-0.09}$
GW151226	$8.9^{+0.3}_{-0.3}$	$0.56^{+0.38}_{-0.33}$	$0.18^{+0.2}_{-0.12}$	$0.49^{+0.39}_{-0.32}$	$0.09^{+0.04}_{-0.04}$
GW170104	$21.4^{+2.2}_{-1.8}$	$0.65^{+0.3}_{-0.23}$	$-0.04^{+0.17}_{-0.21}$	$0.36^{+0.42}_{-0.27}$	$0.2^{+0.08}_{-0.08}$
GW170608	$7.9^{+0.2}_{-0.2}$	$0.69^{+0.28}_{-0.36}$	$0.03^{+0.19}_{-0.07}$	$0.36^{+0.45}_{-0.27}$	$0.07^{+0.02}_{-0.02}$
GW170729	$35.4^{+6.5}_{-4.8}$	$0.68^{+0.28}_{-0.28}$	$0.37^{+0.21}_{-0.25}$	$0.44^{+0.35}_{-0.28}$	$0.49^{+0.19}_{-0.21}$
GW170809	$24.9^{+2.1}_{-1.7}$	$0.68^{+0.28}_{-0.24}$	$0.08^{+0.17}_{-0.17}$	$0.35^{+0.43}_{-0.26}$	$0.2^{+0.05}_{-0.07}$
GW170814	$24.1^{+1.4}_{-1.1}$	$0.83^{+0.15}_{-0.23}$	$0.07^{+0.12}_{-0.12}$	$0.48^{+0.41}_{-0.36}$	$0.12^{+0.03}_{-0.04}$
GW170818	$26.5^{+2.1}_{-1.7}$	$0.76^{+0.21}_{-0.25}$	$-0.09^{+0.18}_{-0.21}$	$0.49^{+0.37}_{-0.34}$	$0.21^{+0.07}_{-0.07}$
GW170823	$29.2^{+4.6}_{-3.6}$	$0.74^{+0.23}_{-0.3}$	$0.09^{+0.22}_{-0.26}$	$0.42^{+0.41}_{-0.31}$	$0.35^{+0.15}_{-0.15}$
GW190408_181802	$18.3^{+1.9}_{-1.2}$	$0.75^{+0.21}_{-0.24}$	$-0.03^{+0.14}_{-0.19}$	$0.39^{+0.37}_{-0.31}$	$0.29^{+0.06}_{-0.1}$
GW190412	$13.3^{+0.4}_{-0.3}$	$0.28^{+0.12}_{-0.06}$	$0.25^{+0.08}_{-0.11}$	$0.3^{+0.19}_{-0.16}$	$0.15^{+0.03}_{-0.03}$
GW190413_052954	$24.6^{+5.5}_{-4.1}$	$0.69^{+0.27}_{-0.29}$	$-0.01^{+0.29}_{-0.34}$	$0.41^{+0.43}_{-0.31}$	$0.59^{+0.29}_{-0.24}$
GW190413_134308	$33.0^{+8.2}_{-5.4}$	$0.69^{+0.28}_{-0.31}$	$-0.03^{+0.25}_{-0.29}$	$0.56^{+0.37}_{-0.41}$	$0.71^{+0.31}_{-0.3}$
GW190421_213856	$31.2^{+5.9}_{-4.2}$	$0.79^{+0.19}_{-0.3}$	$-0.06^{+0.22}_{-0.27}$	$0.48^{+0.4}_{-0.36}$	$0.49^{+0.19}_{-0.21}$
GW190503_185404	$30.2^{+4.2}_{-4.2}$	$0.65^{+0.29}_{-0.23}$	$-0.03^{+0.2}_{-0.26}$	$0.38^{+0.42}_{-0.29}$	$0.27^{+0.11}_{-0.11}$
GW190512_180714	$14.6^{+1.3}_{-1.0}$	$0.54^{+0.37}_{-0.18}$	$0.03^{+0.12}_{-0.13}$	$0.22^{+0.37}_{-0.17}$	$0.27^{+0.09}_{-0.1}$
GW190513_205428	$21.6^{+3.8}_{-1.9}$	$0.5^{+0.42}_{-0.18}$	$0.11^{+0.28}_{-0.17}$	$0.31^{+0.39}_{-0.23}$	$0.37^{+0.13}_{-0.13}$
GW190517_055101	$26.6^{+4.0}_{-4.0}$	$0.68^{+0.27}_{-0.29}$	$0.52^{+0.19}_{-0.19}$	$0.49^{+0.3}_{-0.29}$	$0.34^{+0.24}_{-0.14}$
GW190519_153544	$44.5^{+6.4}_{-7.1}$	$0.61^{+0.28}_{-0.19}$	$0.31^{+0.2}_{-0.22}$	$0.44^{+0.35}_{-0.29}$	$0.44^{+0.25}_{-0.14}$
GW190521_074359	$32.1^{+3.2}_{-2.5}$	$0.78^{+0.19}_{-0.21}$	$0.09^{+0.1}_{-0.13}$	$0.4^{+0.32}_{-0.29}$	$0.24^{+0.07}_{-0.1}$
GW190602_175927	$49.1^{+9.1}_{-8.5}$	$0.71^{+0.25}_{-0.33}$	$0.07^{+0.25}_{-0.24}$	$0.42^{+0.41}_{-0.31}$	$0.47^{+0.25}_{-0.17}$
GW190620_030421	$38.3^{+8.3}_{-6.5}$	$0.62^{+0.32}_{-0.27}$	$0.33^{+0.22}_{-0.25}$	$0.43^{+0.36}_{-0.28}$	$0.49^{+0.23}_{-0.2}$
GW190630_185205	$24.9^{+2.1}_{-2.1}$	$0.68^{+0.27}_{-0.22}$	$0.1^{+0.12}_{-0.13}$	$0.32^{+0.31}_{-0.23}$	$0.18^{+0.1}_{-0.07}$
GW190701_203306	$40.3^{+5.4}_{-4.9}$	$0.76^{+0.21}_{-0.31}$	$-0.07^{+0.23}_{-0.29}$	$0.42^{+0.42}_{-0.31}$	$0.37^{+0.11}_{-0.12}$
GW190706_222641	$42.7^{+10.0}_{-7.0}$	$0.58^{+0.34}_{-0.25}$	$0.28^{+0.26}_{-0.29}$	$0.38^{+0.39}_{-0.28}$	$0.71^{+0.32}_{-0.27}$
GW190707_093326	$8.5^{+0.6}_{-0.5}$	$0.73^{+0.24}_{-0.27}$	$-0.05^{+0.1}_{-0.08}$	$0.29^{+0.39}_{-0.23}$	$0.16^{+0.07}_{-0.07}$
GW190708_232457	$13.2^{+0.9}_{-0.6}$	$0.76^{+0.21}_{-0.28}$	$0.02^{+0.1}_{-0.08}$	$0.29^{+0.43}_{-0.23}$	$0.18^{+0.06}_{-0.07}$
GW190720_000836	$8.9^{+0.5}_{-0.8}$	$0.58^{+0.36}_{-0.3}$	$0.18^{+0.14}_{-0.12}$	$0.33^{+0.43}_{-0.22}$	$0.16^{+0.12}_{-0.06}$
GW190727_060333	$28.6^{+5.3}_{-3.7}$	$0.8^{+0.18}_{-0.32}$	$0.11^{+0.26}_{-0.25}$	$0.47^{+0.41}_{-0.36}$	$0.55^{+0.21}_{-0.22}$
GW190728_064510	$8.6^{+0.5}_{-0.3}$	$0.66^{+0.3}_{-0.37}$	$0.12^{+0.2}_{-0.07}$	$0.29^{+0.37}_{-0.2}$	$0.18^{+0.05}_{-0.07}$
GW190803_022701	$27.3^{+5.7}_{-4.1}$	$0.75^{+0.22}_{-0.31}$	$-0.03^{+0.24}_{-0.27}$	$0.44^{+0.42}_{-0.33}$	$0.55^{+0.26}_{-0.24}$
GW190828_063405	$25.0^{+3.4}_{-2.1}$	$0.82^{+0.15}_{-0.22}$	$0.19^{+0.15}_{-0.16}$	$0.43^{+0.36}_{-0.3}$	$0.38^{+0.1}_{-0.15}$
GW190828_065509	$13.3^{+1.2}_{-1.0}$	$0.43^{+0.38}_{-0.16}$	$0.08^{+0.16}_{-0.16}$	$0.3^{+0.38}_{-0.23}$	$0.3^{+0.1}_{-0.1}$
GW190910_112807	$34.3^{+4.1}_{-4.1}$	$0.82^{+0.15}_{-0.23}$	$0.02^{+0.18}_{-0.18}$	$0.4^{+0.39}_{-0.32}$	$0.28^{+0.16}_{-0.1}$
GW190915_235702	$25.3^{+3.2}_{-2.7}$	$0.69^{+0.27}_{-0.27}$	$0.02^{+0.2}_{-0.25}$	$0.55^{+0.36}_{-0.39}$	$0.3^{+0.11}_{-0.1}$
GW190924_021846	$5.8^{+0.2}_{-0.2}$	$0.57^{+0.36}_{-0.37}$	$0.03^{+0.3}_{-0.09}$	$0.24^{+0.4}_{-0.18}$	$0.12^{+0.04}_{-0.04}$
GW190925_232845	$15.8^{+1.1}_{-1.0}$	$0.73^{+0.24}_{-0.34}$	$0.11^{+0.17}_{-0.14}$	$0.39^{+0.43}_{-0.29}$	$0.19^{+0.07}_{-0.07}$
GW190930_133541	$8.5^{+0.5}_{-0.5}$	$0.64^{+0.3}_{-0.45}$	$0.14^{+0.31}_{-0.15}$	$0.34^{+0.4}_{-0.24}$	$0.15^{+0.06}_{-0.06}$
GW191105_143521	$7.8^{+0.6}_{-0.4}$	$0.72^{+0.24}_{-0.31}$	$-0.02^{+0.13}_{-0.09}$	$0.3^{+0.45}_{-0.24}$	$0.23^{+0.07}_{-0.09}$
GW191109_010717	$47.5^{+9.6}_{-7.5}$	$0.73^{+0.21}_{-0.24}$	$-0.29^{+0.42}_{-0.31}$	$0.63^{+0.29}_{-0.37}$	$0.25^{+0.18}_{-0.12}$
GW191129_134029	$7.3^{+0.4}_{-0.3}$	$0.63^{+0.31}_{-0.29}$	$0.06^{+0.16}_{-0.08}$	$0.26^{+0.36}_{-0.19}$	$0.16^{+0.05}_{-0.06}$
GW191204_171526	$8.6^{+0.4}_{-0.3}$	$0.69^{+0.25}_{-0.26}$	$0.16^{+0.08}_{-0.05}$	$0.39^{+0.35}_{-0.26}$	$0.13^{+0.04}_{-0.05}$
GW191215_223052	$18.4^{+2.2}_{-1.7}$	$0.73^{+0.24}_{-0.27}$	$-0.04^{+0.17}_{-0.21}$	$0.5^{+0.37}_{-0.38}$	$0.35^{+0.13}_{-0.14}$
GW191216_213338	$8.3^{+0.2}_{-0.2}$	$0.64^{+0.31}_{-0.29}$	$0.11^{+0.13}_{-0.06}$	$0.23^{+0.35}_{-0.16}$	$0.07^{+0.02}_{-0.03}$
GW191222_033537	$33.8^{+7.1}_{-5.0}$	$0.79^{+0.18}_{-0.32}$	$-0.04^{+0.2}_{-0.25}$	$0.41^{+0.41}_{-0.32}$	$0.51^{+0.23}_{-0.26}$
GW191230_180458	$36.5^{+8.2}_{-5.6}$	$0.77^{+0.2}_{-0.34}$	$-0.05^{+0.26}_{-0.31}$	$0.52^{+0.38}_{-0.39}$	$0.69^{+0.26}_{-0.27}$
GW200112_155838	$27.4^{+2.6}_{-2.1}$	$0.81^{+0.17}_{-0.26}$	$0.06^{+0.15}_{-0.15}$	$0.39^{+0.39}_{-0.3}$	$0.24^{+0.07}_{-0.08}$
GW200128_022011	$32.0^{+7.5}_{-5.5}$	$0.8^{+0.18}_{-0.3}$	$0.12^{+0.24}_{-0.25}$	$0.57^{+0.34}_{-0.4}$	$0.56^{+0.28}_{-0.28}$
GW200129_065458	$27.2^{+2.1}_{-2.3}$	$0.85^{+0.12}_{-0.41}$	$0.11^{+0.11}_{-0.16}$	$0.52^{+0.42}_{-0.37}$	$0.18^{+0.05}_{-0.07}$
GW200202_154313	$7.5^{+0.2}_{-0.2}$	$0.72^{+0.24}_{-0.31}$	$0.04^{+0.13}_{-0.06}$	$0.28^{+0.4}_{-0.22}$	$0.09^{+0.03}_{-0.03}$
GW200208_130117	$27.7^{+3.6}_{-3.1}$	$0.73^{+0.23}_{-0.29}$	$-0.07^{+0.22}_{-0.27}$	$0.38^{+0.41}_{-0.29}$	$0.4^{+0.15}_{-0.14}$
GW200209_085452	$26.7^{+6.0}_{-4.2}$	$0.78^{+0.19}_{-0.31}$	$-0.12^{+0.24}_{-0.3}$	$0.51^{+0.39}_{-0.37}$	$0.57^{+0.25}_{-0.26}$
GW200219_094415	$27.6^{+5.6}_{-3.8}$	$0.77^{+0.21}_{-0.32}$	$-0.08^{+0.23}_{-0.29}$	$0.48^{+0.4}_{-0.35}$	$0.57^{+0.22}_{-0.22}$
GW200224_222234	$31.1^{+3.2}_{-2.6}$	$0.82^{+0.16}_{-0.26}$	$0.1^{+0.15}_{-0.15}$	$0.49^{+0.37}_{-0.36}$	$0.32^{+0.08}_{-0.11}$
GW200225_060421	$14.2^{+1.5}_{-1.4}$	$0.73^{+0.23}_{-0.28}$	$-0.12^{+0.17}_{-0.28}$	$0.53^{+0.34}_{-0.38}$	$0.22^{+0.09}_{-0.1}$
GW200302_015811	$23.4^{+4.7}_{-3.0}$	$0.53^{+0.36}_{-0.2}$	$0.01^{+0.25}_{-0.26}$	$0.37^{+0.45}_{-0.28}$	$0.28^{+0.16}_{-0.12}$
GW200311_115853	$26.6^{+2.4}_{-2.0}$	$0.82^{+0.16}_{-0.27}$	$-0.02^{+0.16}_{-0.2}$	$0.45^{+0.4}_{-0.35}$	$0.23^{+0.05}_{-0.07}$
GW200316_215756	$8.8^{+0.6}_{-0.6}$	$0.6^{+0.34}_{-0.38}$	$0.13^{+0.27}_{-0.1}$	$0.29^{+0.38}_{-0.2}$	$0.22^{+0.08}_{-0.08}$

References

1. Aasi, J.; Abbott, B.P.; Abbott, R.; Abbott, T.; Abernathy, M.R.; Ackley, K.; Adams, C.; Adams, T.; Addesso, P.; Adhikari, R.X.; et al. Advanced LIGO. *Class. Quantum Gravity* **2015**, *32*, 074001. [CrossRef]
2. Acernese, F.; Agathos, M.; Agatsuma, K.; Aisa, D.; Allemandou, N.; Allocca, A.; Amarni, J.; Astone, P.; Balestri, G.; Ballardin, G.; et al. Advanced Virgo: A second-generation interferometric gravitational wave detector. *Class. Quantum Gravity* **2015**, *32*, 024001. [CrossRef]

3. Abbott, B.P.; Abbott, R.; Abbott, T.D.; Abraham, S.; Acernese, F.; Ackley, K.; Adams, C.; Adhikari, R.X.; Adya, V.B.; Affeldt, C.; et al. GWTC-1: A Gravitational-Wave Transient Catalog of Compact Binary Mergers Observed by LIGO and Virgo during the First and Second Observing Runs. *Phys. Rev. X* **2019**, *9*, 031040. [CrossRef]
4. Abbott, R.; Abbott, T.D.; Abraham, S.; Acernese, F.; Ackley, K.; Adams, A.; Adams, C.; Adhikari, R.X.; Adya, V.B.; Affeldt, C.; et al. GWTC-2: Compact Binary Coalescences Observed by LIGO and Virgo during the First Half of the Third Observing Run. *Phys. Rev. X* **2021**, *11*, 021053. [CrossRef]
5. Abbott, R.; Abbott, T.D.; Acernese, F.; Ackley, K.; Adams, C.; Adhikari, N.; Adhikari, R.X.; Adya, V.B.; Affeldt, C.; Agarwal, D.; et al. GWTC-2.1: Deep Extended Catalog of Compact Binary Coalescences Observed by LIGO and Virgo During the First Half of the Third Observing Run. *arXiv* **2021**, arXiv:2108.01045.
6. Abbott, R.; Abbott, T.D.; Acernese, F.; Ackley, K.; Adams, C.; Adhikari, N.; Adhikari, R.X.; Adya, V.B.; Affeldt, C.; Agarwal, D.; et al. GWTC-3: Compact Binary Coalescences Observed by LIGO and Virgo During the Second Part of the Third Observing Run. *arXiv* **2021**, arXiv:2111.03606.
7. Abbott, R.; Abbott, T.D.; Acernese, F.; Ackley, K.; Adams, C.; Adhikari, N.; Adhikari, R.X.; Adya, V.B.; Affeldt, C.; Agarwal, D.; et al. The population of merging compact binaries inferred using gravitational waves through GWTC-3. *arXiv* **2021**, arXiv:2111.03634.
8. Abbott, R.; Abbott, T.D.; Abraham, S.; Acernese, F.; Ackley, K.; Adams, C.; Adhikari, R.X.; Adya, V.B.; Affeldt, C.; Agathos, M.; et al. GW190412: Observation of a binary-black-hole coalescence with asymmetric masses. *Phys. Rev. D* **2020**, *102*, 043015. [CrossRef]
9. Farr, W.M.; Stevenson, S.; Miller, M.C.; Mandel, I.; Farr, B.; Vecchio, A. Distinguishing spin-aligned and isotropic black hole populations with gravitational waves. *Nature* **2017**, *548*, 426–429. [CrossRef]
10. Farr, B.; Holz, D.E.; Farr, W.M. Using Spin to Understand the Formation of LIGO and Virgo's Black Holes. *ApJL* **2018**, *854*, L9. [CrossRef]
11. Wysocki, D.; Lange, J.; O'Shaughnessy, R. Reconstructing phenomenological distributions of compact binaries via gravitational wave observations. *Phys. Rev. D* **2019**, *100*, 043012. [CrossRef]
12. Roulet, J.; Zaldarriaga, M. Constraints on binary black hole populations from LIGO-Virgo detections. *MNRAS* **2019**, *484*, 4216–4229. [CrossRef]
13. Miller, S.; Callister, T.A.; Farr, W.M. The Low Effective Spin of Binary Black Holes and Implications for Individual Gravitational-wave Events. *ApJL* **2020**, *895*, 128. [CrossRef]
14. Abbott, B.P.; Abbott, R.; Abbott, T.D.; Abernathy, M.R.; Acernese, F.; Ackley, K.; Adams, C.; Adams, T.; Addesso, P.; Adhikari, R.X.; et al. GW151226: Observation of Gravitational Waves from a 22-Solar-Mass Binary Black Hole Coalescence. *Phys. Rev. Lett.* **2016**, *116*, 241103. [CrossRef] [PubMed]
15. Tiwari, V.; Fairhurst, S.; Hannam, M. Constraining Black Hole Spins with Gravitational-wave Observations. *Astrophys. J.* **2018**, *868*, 140. [CrossRef]
16. Venumadhav, T.; Zackay, B.; Roulet, J.; Dai, L.; Zaldarriaga, M. New binary black hole mergers in the second observing run of Advanced LIGO and Advanced Virgo. *Phys. Rev. D* **2020**, *101*, 083030. [CrossRef]
17. Olsen, S.; Venumadhav, T.; Mushkin, J.; Roulet, J.; Zackay, B.; Zaldarriaga, M. New binary black hole mergers in the LIGO-Virgo O3a data. *Phys. Rev. D* **2022**, *106*, 043009. [CrossRef]
18. Callister, T.A.; Farr, W.M.; Renzo, M. State of the Field: Binary Black Hole Natal Kicks and Prospects for Isolated Field Formation after GWTC-2. *Astrophys. J.* **2021**, *920*, 157. [CrossRef]
19. Hoy, C.; Thompson, J.E.; Fairhurst, S.; Raymond, V.; Colleoni, M.; Zimmerman, A. General-relativistic precession in a black-hole binary. *Nature* **2022**, *610*, 652–655. [CrossRef]
20. Callister, T.A.; Miller, S.J.; Chatziioannou, K.; Farr, W.M. No evidence that the majority of black holes in binaries have zero spin. *arXiv* **2022**, arXiv:2205.08574.
21. Gerosa, D.; Kesden, M.; Berti, E.; O'Shaughnessy, R.; Sperhake, U. Resonant-plane locking and spin alignment in stellar-mass black-hole binaries: A diagnostic of compact-binary formation. *Phys. Rev. D* **2013**, *87*, 104028. [CrossRef]
22. Stevenson, S.; Ohme, F.; Fairhurst, S. Distinguishing Compact Binary Population Synthesis Models Using Gravitational Wave Observations of Coalescing Binary Black Holes. *Astrophys. J.* **2015**, *810*, 58. [CrossRef]
23. Rodriguez, C.L.; Zevin, M.; Pankow, C.; Kalogera, V.; Rasio, F.A. Illuminating Black Hole Binary Formation Channels with Spins in Advanced LIGO. *Astrophys. J. Lett.* **2016**, *832*, L2. [CrossRef]
24. Stevenson, S.; Berry, C.P.L.; Mandel, I. Hierarchical analysis of gravitational-wave measurements of binary black hole spin-orbit misalignments. *Mon. Not. R. Astron. Soc.* **2017**, *471*, 2801–2811. [CrossRef]
25. Talbot, C.; Thrane, E. Determining the population properties of spinning black holes. *Phys. Rev. D* **2017**, *96*, 023012. [CrossRef]
26. Fishbach, M.; Holz, D.E. Where Are LIGO's Big Black Holes? *Astrophys. J. Lett.* **2017**, *851*, L25. [CrossRef]
27. Vitale, S.; Lynch, R.; Sturani, R.; Graff, P. Use of gravitational waves to probe the formation channels of compact binaries. *Class. Quantum Gravity* **2017**, *34*, 03LT01. [CrossRef]
28. Zevin, M.; Pankow, C.; Rodriguez, C.L.; Sampson, L.; Chase, E.; Kalogera, V.; Rasio, F.A. Constraining Formation Models of Binary Black Holes with Gravitational-wave Observations. *Astrophys. J.* **2017**, *846*, 82. [CrossRef]

29. Barrett, J.W.; Gaebel, S.M.; Neijssel, C.J.; Vigna-Gómez, A.; Stevenson, S.; Berry, C.P.L.; Farr, W.M.; Mandel, I. Accuracy of inference on the physics of binary evolution from gravitational-wave observations. *Mon. Not. R. Astron. Soc.* **2018**, *477*, 4685–4695. [CrossRef]
30. Taylor, S.R.; Gerosa, D. Mining gravitational-wave catalogs to understand binary stellar evolution: A new hierarchical Bayesian framework. *Phys. Rev. D* **2018**, *98*, 083017. [CrossRef]
31. Fragione, G.; Kocsis, B. Effective spin distribution of black hole mergers in triples. *Mon. Not. R. Astron. Soc.* **2020**, *493*, 3920–3931. [CrossRef]
32. Arca Sedda, M.; Benacquista, M. Using final black hole spins and masses to infer the formation history of the observed population of gravitational wave sources. *Mon. Not. R. Astron. Soc.* **2019**, *482*, 2991–3010. [CrossRef]
33. Bouffanais, Y.; Mapelli, M.; Gerosa, D.; Di Carlo, U.N.; Giacobbo, N.; Berti, E.; Baibhav, V. Constraining the Fraction of Binary Black Holes Formed in Isolation and Young Star Clusters with Gravitational-wave Data. *ApJL* **2019**, *886*, 25. [CrossRef]
34. Bouffanais, Y.; Mapelli, M.; Santoliquido, F.; Giacobbo, N.; Iorio, G.; Costa, G. Constraining accretion efficiency in massive binary stars with LIGO -Virgo black holes. *Mon. Not. R. Astron. Soc.* **2021**, *505*, 3873–3882. [CrossRef]
35. Bouffanais, Y.; Mapelli, M.; Santoliquido, F.; Giacobbo, N.; Di Carlo, U.N.; Rastello, S.; Artale, M.C.; Iorio, G. New insights on binary black hole formation channels after GWTC-2: Young star clusters versus isolated binaries. *Mon. Not. R. Astron. Soc.* **2021**, *507*, 5224–5235. [CrossRef]
36. Kimball, C.; Talbot, C.; Berry, C.P.; Zevin, M.; Thrane, E.; Kalogera, V.; Williams, D. Evidence for Hierarchical Black Hole Mergers in the Second LIGO–Virgo Gravitational Wave Catalog. *Astrophys. J. Lett.* **2021**, *915*, L35. [CrossRef]
37. Kimball, C.; Talbot, C.; Berry, C.P.L.; Carney, M.; Zevin, M.; Thrane, E.; Kalogera, V. Black Hole Genealogy: Identifying Hierarchical Mergers with Gravitational Waves. *ApJL* **2020**, *900*, 177. [CrossRef]
38. Baibhav, V.; Gerosa, D.; Berti, E.; Wong, K.W.K.; Helfer, T.; Mould, M. The mass gap, the spin gap, and the origin of merging binary black holes. *Phys. Rev. D* **2020**, *102*, 043002. [CrossRef]
39. Arca Sedda, M.; Mapelli, M.; Spera, M.; Benacquista, M.; Giacobbo, N. Fingerprints of Binary Black Hole Formation Channels Encoded in the Mass and Spin of Merger Remnants. *Astrophys. J.* **2020**, *894*, 133. [CrossRef]
40. Zevin, M.; Bavera, S.S.; Berry, C.P.L.; Kalogera, V.; Fragos, T.; Marchant, P.; Rodriguez, C.L.; Antonini, F.; Holz, D.E.; Pankow, C. One Channel to Rule Them All? Constraining the Origins of Binary Black Holes Using Multiple Formation Pathways. *Astrophys. J.* **2021**, *910*, 152. [CrossRef]
41. Mapelli, M.; Dall'Amico, M.; Bouffanais, Y.; Giacobbo, N.; Arca Sedda, M.; Artale, M.C.; Ballone, A.; Di Carlo, U.N.; Iorio, G.; Santoliquido, F.; et al. Hierarchical black hole mergers in young, globular and nuclear star clusters: The effect of metallicity, spin and cluster properties. *Mon. Not. R. Astron. Soc.* **2021**, *505*, 339–358. [CrossRef]
42. Mapelli, M.; Bouffanais, Y.; Santoliquido, F.; Arca Sedda, M.; Artale, M.C. The cosmic evolution of binary black holes in young, globular, and nuclear star clusters: Rates, masses, spins, and mixing fractions. *Mon. Not. R. Astron. Soc.* **2022**, *511*, 5797–5816. [CrossRef]
43. Tagawa, H.; Haiman, Z.; Bartos, I.; Kocsis, B.; Omukai, K. Signatures of hierarchical mergers in black hole spin and mass distribution. *Mon. Not. R. Astron. Soc.* **2021**, *507*, 3362–3380. [CrossRef]
44. Gayathri, V.; Yang, Y.; Tagawa, H.; Haiman, Z.; Bartos, I. Black Hole Mergers of AGN Origin in LIGO-Virgo's O1-O3a Observing Periods. *Astrophys. J. Lett.* **2021**, *920*, L42. [CrossRef]
45. Gerosa, D.; Giacobbo, N.; Vecchio, A. High Mass but Low Spin: An Exclusion Region to Rule Out Hierarchical Black Hole Mergers as a Mechanism to Populate the Pair-instability Mass Gap. *Astrophys. J.* **2021**, *915*, 56. [CrossRef]
46. Gompertz, B.P.; Nicholl, M.; Schmidt, P.; Pratten, G.; Vecchio, A. Constraints on compact binary merger evolution from spin-orbit misalignment in gravitational-wave observations. *Mon. Not. R. Astron. Soc.* **2022**, *511*, 1454–1461. [CrossRef]
47. Fryer, C.L.; Kalogera, V. Theoretical Black Hole Mass Distributions. *Astrophys. J.* **2001**, *554*, 548–560. [CrossRef]
48. Heger, A.; Fryer, C.L.; Woosley, S.E.; Langer, N.; Hartmann, D.H. How Massive Single Stars End Their Life. *Astrophys. J.* **2003**, *591*, 288–300. [CrossRef]
49. Belczynski, K.; Bulik, T.; Fryer, C.L.; Ruiter, A.; Valsecchi, F.; Vink, J.S.; Hurley, J.R. On the Maximum Mass of Stellar Black Holes. *Astrophys. J.* **2010**, *714*, 1217–1226. [CrossRef]
50. Mapelli, M.; Zampieri, L.; Ripamonti, E.; Bressan, A. Dynamics of stellar black holes in young star clusters with different metallicities—I. Implications for X-ray binaries. *Mon. Not. R. Astron. Soc.* **2013**, *429*, 2298–2314. [CrossRef]
51. Fragos, T.; McClintock, J.E. The Origin of Black Hole Spin in Galactic Low-mass X-Ray Binaries. *Astrophys. J.* **2015**, *800*, 17. [CrossRef]
52. Marchant, P.; Langer, N.; Podsiadlowski, P.; Tauris, T.M.; Moriya, T.J. A new route towards merging massive black holes. *Astron. Astrophys.* **2016**, *588*, A50. [CrossRef]
53. Eldridge, J.J.; Stanway, E.R. BPASS predictions for binary black hole mergers. *Mon. Not. R. Astron. Soc.* **2016**, *462*, 3302–3313. [CrossRef]
54. De Mink, S.E.; Mandel, I. The chemically homogeneous evolutionary channel for binary black hole mergers: Rates and properties of gravitational-wave events detectable by advanced LIGO. *Mon. Not. R. Astron. Soc.* **2016**, *460*, 3545–3553. [CrossRef]
55. Spera, M.; Mapelli, M. Very massive stars, pair-instability supernovae and intermediate-mass black holes with the sevn code. *Mon. Not. R. Astron. Soc.* **2017**, *470*, 4739–4749. [CrossRef]

56. Bavera, S.S.; Fragos, T.; Qin, Y.; Zapartas, E.; Neijssel, C.J.; Mandel, I.; Batta, A.; Gaebel, S.M.; Kimball, C.; Stevenson, S. The origin of spin in binary black holes. Predicting the distributions of the main observables of Advanced LIGO. *Astron. Astrophys.* **2020**, *635*, A97. [CrossRef]
57. Belczynski, K.; Klencki, J.; Fields, C.E.; Olejak, A.; Berti, E.; Meynet, G.; Fryer, C.L.; Holz, D.E.; O'Shaughnessy, R.; Brown, D.A.; et al. Evolutionary roads leading to low effective spins, high black hole masses, and O1/O2 rates for LIGO/Virgo binary black holes. *Astron. Astrophys.* **2020**, *636*, A104. [CrossRef]
58. Fragione, G.; Kocsis, B.; Rasio, F.A.; Silk, J. Repeated Mergers, Mass-gap Black Holes, and Formation of Intermediate-mass Black Holes in Dense Massive Star Clusters. *Astrophys. J.* **2022**, *927*, 231. [CrossRef]
59. Mandel, I.; Müller, B.; Riley, J.; de Mink, S.E.; Vigna-Gómez, A.; Chattopadhyay, D. Binary population synthesis with probabilistic remnant mass and kick prescriptions. *Mon. Not. R. Astron. Soc.* **2021**, *500*, 1380–1384. [CrossRef]
60. Fryer, C.L.; Olejak, A.; Belczynski, K. The Effect of Supernova Convection On Neutron Star and Black Hole Masses. *Astrophys. J.* **2022**, *931*, 94. [CrossRef]
61. Olejak, A.; Fryer, C.L.; Belczynski, K.; Baibhav, V. The role of supernova convection for the lower mass gap in the isolated binary formation of gravitational wave sources. *Mon. Not. R. Astron. Soc.* **2022**, *516*, 2252–2271. [CrossRef]
62. Chattopadhyay, D.; Hurley, J.; Stevenson, S.; Raidani, A. Dynamical double black holes and their host cluster properties. *Mon. Not. R. Astron. Soc.* **2022**, *513*, 4527–4555. [CrossRef]
63. van Son, L.A.C.; de Mink, S.E.; Renzo, M.; Justham, S.; Zapartas, E.; Breivik, K.; Callister, T.; Farr, W.M.; Conroy, C. No Peaks without Valleys: The Stable Mass Transfer Channel for Gravitational-wave Sources in Light of the Neutron Star—Black Hole Mass Gap. *Astrophys. J.* **2022**, *940*, 184. [CrossRef]
64. Briel, M.M.; Stevance, H.F.; Eldridge, J.J. Understanding the high-mass binary black hole population from stable mass transfer and super-Eddington accretion in BPASS. *arXiv* **2022**, arXiv:2206.13842.
65. Stevenson, S.; Clarke, T.A. Constraints on the contributions to the observed binary black hole population from individual evolutionary pathways in isolated binary evolution. *Mon. Not. R. Astron. Soc.* **2022**. [CrossRef]
66. Broekgaarden, F.S.; Berger, E.; Stevenson, S.; Justham, S.; Mandel, I.; Chruślińska, M.; van Son, L.A.C.; Wagg, T.; Vigna-Gómez, A.; de Mink, S.E.; et al. Impact of massive binary star and cosmic evolution on gravitational wave observations—II. Double compact object rates and properties. *Mon. Not. R. Astron. Soc.* **2022**, *516*, 5737–5761. [CrossRef]
67. Broekgaarden, F.S.; Stevenson, S.; Thrane, E. Signatures of Mass Ratio Reversal in Gravitational Waves from Merging Binary Black Holes. *Astrophys. J.* **2022**, *938*, 45. [CrossRef]
68. Qin, Y.; Fragos, T.; Meynet, G.; Andrews, J.; Sørensen, M.; Song, H.F. The spin of the second-born black hole in coalescing binary black holes. *Astron. Astrophys.* **2018**, *616*, A28. [CrossRef]
69. Qin, Y.; Fragos, T.; Meynet, G.; Marchant, P.; Kalogera, V.; Andrews, J.; Sørensen, M.; Song, H.F. The black hole spin in coalescing binary black holes and high-mass X-ray binaries. *IAU Symposium* **2019**, *346*, 426–432. [CrossRef]
70. Fuller, J.; Ma, L. Most Black Holes Are Born Very Slowly Rotating. *Astrophys. J. Lett.* **2019**, *881*, L1. [CrossRef]
71. Olejak, A.; Belczynski, K. The Implications of High Black Hole Spins for the Origin of Binary Black Hole Mergers. *Astrophys. J. Lett.* **2021**, *921*, L2. [CrossRef]
72. Stevenson, S. Biases in Estimates of Black Hole Kicks from the Spin Distribution of Binary Black Holes. *Astrophys. J. Lett.* **2022**, *926*, L32. [CrossRef]
73. Maeder, A.; Meynet, G. The Evolution of Rotating Stars. *Ann. Rev. Astron. Astrophys.* **2000**, *38*, 143–190. [CrossRef]
74. Cantiello, M.; Mankovich, C.; Bildsten, L.; Christensen-Dalsgaard, J.; Paxton, B. Angular Momentum Transport within Evolved Low-mass Stars. *Astrophys. J.* **2014**, *788*, 93. [CrossRef]
75. Fuller, J.; Piro, A.L.; Jermyn, A.S. Slowing the spins of stellar cores. *Mon. Not. R. Astron. Soc.* **2019**, *485*, 3661–3680. [CrossRef]
76. Zahn, J.P. Circulation and turbulence in rotating stars. *Astron. Astrophys.* **1992**, *265*, 115–132.
77. Ekström, S.; Georgy, C.; Eggenberger, P.; Meynet, G.; Mowlavi, N.; Wyttenbach, A.; Granada, A.; Decressin, T.; Hirschi, R.; Frischknecht, U.; et al. Grids of stellar models with rotation. I. Models from 0.8 to 120 $M_{\odot}$ at solar metallicity (Z = 0.014). *Astron. Astrophys.* **2012**, *537*, A146. [CrossRef]
78. Limongi, M.; Chieffi, A. Presupernova Evolution and Explosive Nucleosynthesis of Rotating Massive Stars in the Metallicity Range $-3 \leq [\mathrm{Fe/H}] \leq 0$. *Astrophys. J. Suppl.* **2018**, *237*, 13. [CrossRef]
79. Costa, G.; Girardi, L.; Bressan, A.; Marigo, P.; Rodrigues, T.S.; Chen, Y.; Lanza, A.; Goudfrooij, P. Mixing by overshooting and rotation in intermediate-mass stars. *Mon. Not. R. Astron. Soc.* **2019**, *485*, 4641–4657. [CrossRef]
80. Spruit, H.C. Dynamo action by differential rotation in a stably stratified stellar interior. *Astron. Astrophys.* **2002**, *381*, 923–932. [CrossRef]
81. Mosser, B.; Goupil, M.J.; Belkacem, K.; Marques, J.P.; Beck, P.G.; Bloemen, S.; De Ridder, J.; Barban, C.; Deheuvels, S.; Elsworth, Y.; et al. Spin down of the core rotation in red giants. *Astron. Astrophys.* **2012**, *548*, A10. [CrossRef]
82. Gehan, C.; Mosser, B.; Michel, E.; Samadi, R.; Kallinger, T. Core rotation braking on the red giant branch for various mass ranges. *Astron. Astrophys.* **2018**, *616*, A24. [CrossRef]
83. Aerts, C.; Mathis, S.; Rogers, T.M. Angular Momentum Transport in Stellar Interiors. *Ann. Rev. Astron. Astrophys.* **2019**, *57*, 35–78. [CrossRef]
84. Reynolds, C.S. Observational Constraints on Black Hole Spin. *Ann. Rev. Astron. Astrophys.* **2021**, *59*, 117–154. [CrossRef]

85. Miller-Jones, J.C.A.; Bahramian, A.; Orosz, J.A.; Mandel, I.; Gou, L.; Maccarone, T.J.; Neijssel, C.J.; Zhao, X.; Ziółkowski, J.; Reid, M.J.; et al. Cygnus X-1 contains a 21-solar mass black hole—Implications for massive star winds. *Science* **2021**, *371*, 1046–1049. [CrossRef]
86. Fishbach, M.; Kalogera, V. Apples and Oranges: Comparing Black Holes in X-ray Binaries and Gravitational-wave Sources. *Astrophys. J. Lett.* **2022**, *929*, L26. [CrossRef]
87. Shafee, R.; McClintock, J.E.; Narayan, R.; Davis, S.W.; Li, L.X.; Remillard, R.A. Estimating the Spin of Stellar-Mass Black Holes by Spectral Fitting of the X-ray Continuum. *Astrophys. J.* **2006**, *636*, L113–L116. [CrossRef]
88. Motta, S.E.; Belloni, T.M.; Stella, L.; Muñoz-Darias, T.; Fender, R. Precise mass and spin measurements for a stellar-mass black hole through X-ray timing: The case of GRO J1655-40. *Mon. Not. R. Astron. Soc.* **2014**, *437*, 2554–2565. [CrossRef]
89. Kushnir, D.; Zaldarriaga, M.; Kollmeier, J.A.; Waldman, R. GW150914: Spin-based constraints on the merger time of the progenitor system. *Mon. Not. R. Astron. Soc.* **2016**, *462*, 844–849. [CrossRef]
90. Hotokezaka, K.; Piran, T. Implications of the Low Binary Black Hole Aligned Spins Observed by LIGO. *Astrophys. J.* **2017**, *842*, 111. [CrossRef]
91. Zaldarriaga, M.; Kushnir, D.; Kollmeier, J.A. The expected spins of gravitational wave sources with isolated field binary progenitors. *Mon. Not. R. Astron. Soc.* **2018**, *473*, 4174–4178. [CrossRef]
92. Gerosa, D.; Berti, E.; O'Shaughnessy, R.; Belczynski, K.; Kesden, M.; Wysocki, D.; Gladysz, W. Spin orientations of merging black holes formed from the evolution of stellar binaries. *Phys. Rev. D* **2018**, *98*, 084036. [CrossRef]
93. Stegmann, J.; Antonini, F. Flipping spins in mass transferring binaries and origin of spin-orbit misalignment in binary black holes. *Phys. Rev. D* **2021**, *103*, 063007. [CrossRef]
94. Kalogera, V. Spin-Orbit Misalignment in Close Binaries with Two Compact Objects. *Astrophys. J.* **2000**, *541*, 319–328. [CrossRef]
95. Mapelli, M.; Giacobbo, N.; Ripamonti, E.; Spera, M. The cosmic merger rate of stellar black hole binaries from the Illustris simulation. *Mon. Not. R. Astron. Soc.* **2017**, *472*, 2422–2435. [CrossRef]
96. Giacobbo, N.; Mapelli, M.; Spera, M. Merging black hole binaries: The effects of progenitor's metallicity, mass-loss rate and Eddington factor. *Mon. Not. R. Astron. Soc.* **2018**, *474*, 2959–2974. [CrossRef]
97. Hurley, J.R.; Pols, O.R.; Tout, C.A. Comprehensive analytic formulae for stellar evolution as a function of mass and metallicity. *Mon. Not. R. Astron. Soc.* **2000**, *315*, 543–569. [CrossRef]
98. Hurley, J.R.; Tout, C.A.; Pols, O.R. Evolution of binary stars and the effect of tides on binary populations. *Mon. Not. R. Astron. Soc.* **2002**, *329*, 897–928. [CrossRef]
99. Vink, J.S.; de Koter, A.; Lamers, H.J.G.L.M. Mass-loss predictions for O and B stars as a function of metallicity. *Astron. Astrophys.* **2001**, *369*, 574–588. [CrossRef]
100. Giacobbo, N.; Mapelli, M. The progenitors of compact-object binaries: Impact of metallicity, common envelope and natal kicks. *Mon. Not. R. Astron. Soc.* **2018**, *480*, 2011–2030. [CrossRef]
101. Giacobbo, N.; Mapelli, M. The impact of electron-capture supernovae on merging double neutron stars. *Mon. Not. R. Astron. Soc.* **2019**, *482*, 2234–2243. [CrossRef]
102. Fryer, C.L.; Belczynski, K.; Wiktorowicz, G.; Dominik, M.; Kalogera, V.; Holz, D.E. Compact Remnant Mass Function: Dependence on the Explosion Mechanism and Metallicity. *Astrophys. J.* **2012**, *749*, 91. [CrossRef]
103. Mapelli, M.; Spera, M.; Montanari, E.; Limongi, M.; Chieffi, A.; Giacobbo, N.; Bressan, A.; Bouffanais, Y. Impact of the Rotation and Compactness of Progenitors on the Mass of Black Holes. *Astrophys. J.* **2020**, *888*, 76. [CrossRef]
104. Özel, F.; Psaltis, D.; Narayan, R.; McClintock, J.E. The Black Hole Mass Distribution in the Galaxy. *Astrophys. J.* **2010**, *725*, 1918–1927. [CrossRef]
105. Farr, W.M.; Sravan, N.; Cantrell, A.; Kreidberg, L.; Bailyn, C.D.; Mandel, I.; Kalogera, V. The Mass Distribution of Stellar-mass Black Holes. *Astrophys. J.* **2011**, *741*, 103. [CrossRef]
106. Bray, J.C.; Eldridge, J.J. Neutron star kicks and their relationship to supernovae ejecta mass. *Mon. Not. R. Astron. Soc.* **2016**, *461*, 3747–3759. [CrossRef]
107. Bray, J.C.; Eldridge, J.J. Neutron star kicks-II. Revision and further testing of the conservation of momentum 'kick' model. *Mon. Not. R. Astron. Soc.* **2018**, *480*, 5657–5672. [CrossRef]
108. Giacobbo, N.; Mapelli, M. Revising Natal Kick Prescriptions in Population Synthesis Simulations. *Astrophys. J.* **2020**, *891*, 141. [CrossRef]
109. Tauris, T.M.; Langer, N.; Podsiadlowski, P. Ultra-stripped supernovae: Progenitors and fate. *Mon. Not. R. Astron. Soc.* **2015**, *451*, 2123–2144. [CrossRef]
110. Tauris, T.M.; Kramer, M.; Freire, P.C.C.; Wex, N.; Janka, H.T.; Langer, N.; Podsiadlowski, P.; Bozzo, E.; Chaty, S.; Kruckow, M.U.; et al. Formation of Double Neutron Star Systems. *Astrophys. J.* **2017**, *846*, 170. [CrossRef]
111. Hobbs, G.; Lorimer, D.R.; Lyne, A.G.; Kramer, M. A statistical study of 233 pulsar proper motions. *Mon. Not. R. Astron. Soc.* **2005**, *360*, 974–992. [CrossRef]
112. Repetto, S.; Igoshev, A.P.; Nelemans, G. The Galactic distribution of X-ray binaries and its implications for compact object formation and natal kicks. *Mon. Not. R. Astron. Soc.* **2017**, *467*, 298–310. [CrossRef]
113. Atri, P.; Miller-Jones, J.C.A.; Bahramian, A.; Plotkin, R.M.; Jonker, P.G.; Nelemans, G.; Maccarone, T.J.; Sivakoff, G.R.; Deller, A.T.; Chaty, S.; et al. Potential kick velocity distribution of black hole X-ray binaries and implications for natal kicks. *Mon. Not. R. Astron. Soc.* **2019**, *489*, 3116–3134. [CrossRef]

114. Hut, P. Tidal evolution in close binary systems. *Astron. Astrophys.* **1981**, *99*, 126–140.
115. Bavera, S.S.; Zevin, M.; Fragos, T. Approximations of the Spin of Close Black Hole-Wolf-Rayet Binaries. *Res. Notes Am. Astron. Soc.* **2021**, *5*, 127. [CrossRef]
116. Maccarone, T.J.; Kundu, A.; Zepf, S.E.; Rhode, K.L. A black hole in a globular cluster. *Nature* **2007**, *445*, 183–185. [CrossRef]
117. Paxton, B.; Schwab, J.; Bauer, E.B.; Bildsten, L.; Blinnikov, S.; Duffell, P.; Farmer, R.; Goldberg, J.A.; Marchant, P.; Sorokina, E.; et al. Modules for Experiments in Stellar Astrophysics (MESA): Convective Boundaries, Element Diffusion, and Massive Star Explosions. *Astrophys. J. Suppl.* **2018**, *234*, 34. [CrossRef]
118. Kroupa, P. On the variation of the initial mass function. *Mon. Not. R. Astron. Soc.* **2001**, *322*, 231–246. [CrossRef]
119. Santoliquido, F.; Mapelli, M.; Giacobbo, N.; Bouffanais, Y.; Artale, M.C. The cosmic merger rate density of compact objects: Impact of star formation, metallicity, initial mass function, and binary evolution. *Mon. Not. R. Astron. Soc.* **2021**, *502*, 4877–4889. [CrossRef]
120. Sana, H.; de Mink, S.E.; de Koter, A.; Langer, N.; Evans, C.J.; Gieles, M.; Gosset, E.; Izzard, R.G.; Le Bouquin, J.B.; Schneider, F.R.N. Binary Interaction Dominates the Evolution of Massive Stars. *Science* **2012**, *337*, 444. [CrossRef]
121. Claeys, J.S.W.; Pols, O.R.; Izzard, R.G.; Vink, J.; Verbunt, F.W.M. Theoretical uncertainties of the Type Ia supernova rate. *Astron. Astrophys.* **2014**, *563*, A83. [CrossRef]
122. Iorio, G.; Mapelli, M.; Costa, G.; Spera, M.; Escobar, G.J.; Sgalletta, C.; Trani, A.A.; Korb, E.; Santoliquido, F.; Dall'Amico, M.; et al. Compact object mergers: Exploring uncertainties from stellar and binary evolution with SEVN. *Mon. Not. R. Astron. Soc.* **2023**, *524*, 426–470. [CrossRef]
123. Santoliquido, F.; Mapelli, M.; Bouffanais, Y.; Giacobbo, N.; Di Carlo, U.N.; Rastello, S.; Artale, M.C.; Ballone, A. The Cosmic Merger Rate Density Evolution of Compact Binaries Formed in Young Star Clusters and in Isolated Binaries. *Astrophys. J.* **2020**, *898*, 152. [CrossRef]
124. Aghanim, N.; Akrami, Y.; Ashdown, M.; Aumont, J.; Baccigalupi, C.; Ballardini, M.; Banday, A.J.; Barreiro, R.B.; Bartolo, N.; Basak, S.; et al. Planck 2018 results. VI. Cosmological parameters. *Astron. Astrophys.* **2020**, *641*, A6. [CrossRef]
125. Madau, P.; Fragos, T. Radiation Backgrounds at Cosmic Dawn: X-rays from Compact Binaries. *Astrophys. J.* **2017**, *840*, 39. [CrossRef]
126. Loredo, T.J. Accounting for Source Uncertainties in Analyses of Astronomical Survey Data. In Proceedings of the Bayesian Inference and Maximum Entropy Methods in Science and Engineering: 24th International Workshop on Bayesian Inference and Maximum Entropy Methods in Science and Engineering, Garching, Germany, 25–30 July 2004; Fischer, R., Preuss, R., Toussaint, U.V., Eds.; American Institute of Physics Conference Series; Volume 735, pp. 195–206. [CrossRef]
127. Mandel, I.; Farr, W.M.; Gair, J.R. Extracting distribution parameters from multiple uncertain observations with selection biases. *Mon. Not. R. Astron. Soc.* **2019**, *486*, 1086–1093. [CrossRef]
128. Thrane, E.; Talbot, C. An introduction to Bayesian inference in gravitational-wave astronomy: Parameter estimation, model selection, and hierarchical models. *Pub. Astron. Soc. Aus.* **2019**, *36*, e010. [CrossRef]
129. Patton, R.A.; Sukhbold, T.; Eldridge, J.J. Comparing compact object distributions from mass- and presupernova core structure-based prescriptions. *Mon. Not. R. Astron. Soc.* **2022**, *511*, 903–913. [CrossRef]
130. Schneider, F.R.N.; Podsiadlowski, P.; Laplace, E. Bimodal Black Hole Mass Distribution and Chirp Masses of Binary Black Hole Mergers. *Astrophys. J. Lett.* **2023**, *950*, L9. [CrossRef]
131. Di Carlo, U.N.; Giacobbo, N.; Mapelli, M.; Pasquato, M.; Spera, M.; Wang, L.; Haardt, F. Merging black holes in young star clusters. *Mon. Not. R. Astron. Soc.* **2019**, *487*, 2947–2960. [CrossRef]
132. Dall'Amico, M.; Mapelli, M.; Di Carlo, U.N.; Bouffanais, Y.; Rastello, S.; Santoliquido, F.; Ballone, A.; Arca Sedda, M. GW190521 formation via three-body encounters in young massive star clusters. *Mon. Not. R. Astron. Soc.* **2021**, *508*, 3045–3054. [CrossRef]
133. Antonini, F.; Gieles, M.; Dosopoulou, F.; Chattopadhyay, D. Coalescing black hole binaries from globular clusters: Mass distributions and comparison to gravitational wave data from GWTC-3. *Mon. Not. R. Astron. Soc.* **2023**, *522*, 466–476. [CrossRef]
134. Biscoveanu, S.; Isi, M.; Vitale, S.; Varma, V. New Spin on LIGO-Virgo Binary Black Holes. *Phys. Rev. Lett.* **2021**, *126*, 171103. [CrossRef] [PubMed]
135. Roulet, J.; Chia, H.S.; Olsen, S.; Dai, L.; Venumadhav, T.; Zackay, B.; Zaldarriaga, M. Distribution of effective spins and masses of binary black holes from the LIGO and Virgo O1-O3a observing runs. *Phys. Rev. D* **2021**, *104*, 083010. [CrossRef]
136. Galaudage, S.; Talbot, C.; Nagar, T.; Jain, D.; Thrane, E.; Mandel, I. Building Better Spin Models for Merging Binary Black Holes: Evidence for Nonspinning and Rapidly Spinning Nearly Aligned Subpopulations. *Astrophys. J. Lett.* **2021**, *921*, L15. [CrossRef]
137. Tong, H.; Galaudage, S.; Thrane, E. Population properties of spinning black holes using the gravitational-wave transient catalog 3. *Phys. Rev. D* **2022**, *106*, 103019. [CrossRef]
138. Abbott, T.D.; Abraham, S.; Acernese, F.; Ackley, K.; Adams, C.; Buikema, A.; Adhikari, R.X.; Adya, V.B.; Affeldt, C.; Agathos, M.; et al. Open data from the first and second observing runs of Advanced LIGO and Advanced Virgo. *SoftwareX* **2021**, *13*, 100658. [CrossRef]
139. Abbott, R.; Abe, H.; Acernese, F.; Ackley, K.; Adhicary, S.; Adhikari, N.; Adhikari, R.X.; et al. [The LIGO Scientific Collaboration, The Virgo Collaboration, The KAGRA Collaboration]. Open data from the third observing run of LIGO, Virgo, KAGRA and GEO. *arXiv* **2023**, arXiv:2302.03676.
140. Harris, C.R.; Millman, K.J.; van der Walt, S.J.; Gommers, R.; Virtanen, P.; Cournapeau, D.; Wieser, E.; Taylor, J.; Berg, S.; Smith, N.J.; et al. Array programming with NumPy. *Nature* **2020**, *585*, 357–362. [CrossRef]

141. Virtanen, P.; Gommers, R.; Oliphant, T.E.; Haberland, M.; Reddy, T.; Cournapeau, D.; Burovski, E.; Peterson, P.; Weckesser, W.; Bright, J.; et al. SciPy 1.0: Fundamental Algorithms for Scientific Computing in Python. *Nat. Methods* **2020**, *17*, 261–272. [CrossRef]
142. Hunter, J.D. Matplotlib: A 2D graphics environment. *Comput. Sci. Eng.* **2007**, *9*, 90–95. [CrossRef]